Electrochimica Acta 490 (2024) 144270

Contents lists available at ScienceDirect

Electrochimica Acta

journal homepage: www.journals.elsevier.com/electrochimica-acta

Unveiling the kinetics of CO_2 reduction in aprotic electrolyte: The critical role of adsorption

Niklas Oppel [a], Philipp Röse [a], Stephan Heuser [b], Michael Prokein [b], Ulf-Peter Apfel [b,c], Ulrike Krewer [a,*]

[a] Institute for Applied Materials – Electrochemical Technologies, Karlsruhe Institute of Technology, Adenauerring 20b, Karlsruhe 76131, Germany
[b] Fraunhofer Institute for Environmental, Safety and Energy Technology UMSICHT, Osterfelder Straße 3, Oberhausen 46047, Germany
[c] Inorganic Chemistry I – Technical Electrochemistry, Ruhr University Bochum, Universitätsstraße 150, Bochum 44801, Germany

ARTICLE INFO

Keywords:
Copper
Cyclic voltammetry
Electrocatalysis
Kinetic modeling
Operating conditions

ABSTRACT

Aprotic organic electrolytes for electrocatalytic CO_2 reduction (CO_2R) offer a promising yet little-explored alternative to avoid the selectivity issues of alkaline media. We present a model-assisted study of the local reaction environment at a Cu cathode in aprotic organic electrolytes to determine the kinetics of the CO_2R and the kinetic limitations and reveal their dependence on reaction conditions. The adsorption of CO_2 is identified as the rate-determining step, as opposed to the often-assumed electron transfer during radical anion formation. Unlike alkaline media, there is no transport limitation in aprotic media. Furthermore, our model predicts two strategies to overcome the adsorption limitation: (i) by increasing surface roughness and (ii) by elevating pressure. The findings highlight the critical role of CO_2 adsorption on CO_2R performance and enable knowledge-driven optimization of reaction conditions and electrocatalysts.

1. Introduction

The electrocatalytic CO_2 reduction (CO_2R) on Cu-based electrocatalysts offers a promising solution to mitigate greenhouse gas emissions by converting CO_2 into valuable fuels and chemicals [1,2]. Apart from the electrode material, the choice of electrolyte is essential for determining the efficiency and selectivity of CO_2R [3,4]. Aqueous electrolytes have been widely studied for their availability, low cost, and environmental safety [5,6]. However, their use leads to several limitations, including operational instability of the Cu surface [7–9], low product selectivity for Cu-based electrodes [10,11], low CO_2 solubility and thus CO_2 transport limitations [12,13], loss of CO_2 to alkaline carbonate formation [14,15], and the competing hydrogen evolution reaction (HER) [16,17]. In order to suppress HER and improve product selectivity, the use of aprotic organic electrolytes with Cu electrodes has been proposed as they have higher CO_2 solubility and allow for the precise control of proton availability [18,19]. Recently, Chu and Surendranath demonstrated the use of phenol as a proton donor for CO electroreduction and produced ethylene with faradaic efficiency (FE) > 15 % [20]. CO_2R in aprotic electrolytes is thus a highly attractive alternative to the widely studied aqueous CO_2R.

Previous research using aprotic electrolytes in CO_2R has focused primarily on experimental studies [21–29]. Modeling efforts are limited to a few microkinetic [30,31] and process studies [32], with only a single publication addressing reaction and transport effects [33]. Furthermore, analyses are typically done under stationary conditions, neglecting transient effects and the advantage of electrochemical energy conversion technologies to adjust to the varying renewable energy supply [34].

CO_2 reduction in dry aprotic solvents differs from that in aqueous solution, as it mainly yields CO and carbonate or oxalate [35]. Small amounts of H_2 and formate originate from protons from residual water [36–38]. Amatore and Savéant propose a reaction mechanism that involves the formation of a CO_2 radical anion [39], which requires high overpotentials [36], and is, thus, considered the rate-determining step [37]. The radical anion can react either by desorbing and dimerizing with another CO_2 radical anion to oxalate via C—C coupling (Fig. 1, Pathway A) or by reacting with another CO_2 molecule (Pathway B). This step is thought to go via the formation of the carbonic formic anhydride radical anion, which, to the best of our knowledge, has not been experimentally confirmed yet. Following a second electron transfer, the adduct disproportionates into carbon monoxide and carbonate [39]. The selectivity towards the two pathways is still debated but thought to be

* Corresponding author.
E-mail address: ulrike.krewer@kit.edu (U. Krewer).

https://doi.org/10.1016/j.electacta.2024.144270
Received 13 February 2024; Received in revised form 9 April 2024; Accepted 13 April 2024
Available online 17 April 2024

determined by the cathode's binding affinity towards the $CO_2/CO_2^{\bullet-}$ couple: A weak interaction between the cathode and the CO_2 adsorbate as on Hg and Pb leads to a preference of oxalate formation in the electrolyte bulk, while strong $CO_2/CO_2^{\bullet-}$ binding as on Cu and Ag, favor the carbon monoxide pathway [40]. Studies on metallic Cu in acetonitrile by Ikeda et al. showed high selectivity for CO with FE > 75 % and no oxalate formation [23]. Later, Figueiredo and coworkers confirmed the absence of oxalate formation on Cu in acetonitrile by in situ Raman and FTIR experiments [36]. Bagger and coworkers used a microkinetic model based on binding energies from density functional theory (DFT) to predict the product distribution of CO_2R in aprotic electrolytes for various transition metals [31]. While their model could not explain the experimental trends for Cu reported by Ikeda et al., their study provided further mechanistic insight into the CO pathway, which most likely proceeds through a single adsorbed CO_2 and a second CO_2 from solution rather than through two neighboring adsorbed $*CO_2$ and $*CO_2^{\bullet-}$ intermediates.

In addition to the electrode material, the choice of solvent impacts the CO_2 reduction. The most commonly used aprotic solvent is acetonitrile [41], which has an 8-fold higher solubility for CO_2 than water at standard conditions [42], a broad electrochemical stability window [40], and shows the highest activity for CO_2R [24]. Furthermore, acetonitrile seems to favor the CO pathway over oxalate formation, attributed to its low donor number, i.e., low nucleophilicity. More nucleophile solvents, such as dimethylformamide and dimethyl sulfoxide, stabilize the $CO_2^{\bullet-}$ radical intermediate in solution, thus promoting oxalate formation [33].

Supporting salts, typically tetraalkylammonium salts, are employed to enhance ionic conductivity. They possess reasonable electrochemical stability and solubility in organic solvents [24]. Additionally, R_4N^+-salts, especially with smaller alkyl chains, stabilize the $CO_2^{\bullet-}$ radical anion [43]. On the other hand, alkali cations inhibit CO_2R in aprotic electrolytes by forming a protective carbonate layer on the electrode surface which prevents further electrochemical reactions [29].

To date, it remains to be determined whether CO_2 transport in the liquid electrolyte, CO_2 adsorption or product desorption from the electrode surface, electrochemical reactions, or chemical reaction steps at the surface limit the overall performance, facilitate cathodic Cu corrosion and must be addressed to elevate CO_2 electrolysis to become a cornerstone of CO_2 utilization and aid in the defossilization of the process industry.

This publication addresses this question by scrutinizing the reaction and transport kinetics of the CO_2R at Cu in acetonitrile. It employs a dynamic kinetic model of the reaction during cyclic voltammetry (CV) experiments. Dynamic electrochemical methods, especially CV, have proven in the past to be highly effective in identifying proper microkinetic models and parameters [44,45], macrokinetic effects [46,47], and catalyst degradation [48,49]. Our prior CV modeling study of CO_2R on Ag in alkaline electrolytes revealed that CO_2R is hampered by slow transport, affecting local pH and CO_2 availability [47]. Therefore, in this study, the impact of CO_2 transport in aprotic electrolytes is investigated and compared to possible microkinetic limitations. We provide significant insights into the local reaction processes and the dominating kinetics and propose design and operating measures to enhance CO_2R performance.

2. Experimental details

2.1. Cyclic voltammetry at ambient conditions

Cyclic voltammetry (CV) experiments were conducted at ambient conditions (25 °C, 101.3 kPa) in a three-electrode glass cell using a *Gamry Interface 1010E* and *Gamry Reference 600+* potentiostat. 150 mL of 0.1 mol L^{-1} tetra-*N*-butylammonium tetrafluoroborate ($TBABF_4$) in acetonitrile electrolyte solution was prepared with $TBABF_4$ 98 % (*abcr GmbH*) and analytic grade dry acetonitrile (*Merck Supelco®*, max. 10 ppm H_2O). A planar Copper disk ($A = 0.1963$ cm^2) made from copper rod (99.999 %, *Fisher Scientific GmbH*) in a PEEK shroud RDE tip holder (*Pine Research Instrumentation Inc.*) was used as the working electrode. The working electrode was polished prior to the experiment with 0.25 µm diamond paste (*Kemet International Ltd.*) A coiled Pt-wire inserted in a glass tube with a porous glass frit at the bottom served as the counter electrode. Ag/AgCl (KCl_{sat} in H_2O) reference electrode (*Sensortechnik Meinsberg*) was used, and all given potentials are referenced to it. Neither the solution was stirred, nor the working electrode rotated.

To obtain CO_2 saturated electrolyte, CO_2 gas (≥ 99.995 %, *Air Liquide Deutschland GmbH*) was fed into the electrolyte for at least 15 min prior to the measurement at a constant flow rate of 60 mL min^{-1} through a fritted bubbler. During the measurement, bubbling was stopped, and in turn, a CO_2 gas atmosphere was maintained above the solution using a flow of 30 mL min^{-1}.

At the start of each measurement, a preconditioning step consisting of 20 consecutive cyclic voltammetry cycles at 100 mV s^{-1} between –0.8 V and –2.4 V was performed. Then, cyclic voltammograms for five consecutive cycles were recorded for each of the following scan rates: 300 mV s^{-1}, 200 mV s^{-1}, 100 mV s^{-1}, and 50 mV s^{-1} in descending order, sweeping between the starting potential of –0.8 V and –2.4 V. The potential limits were chosen to avoid copper oxidation at potentials above −0.8 V and electrolyte decomposition below −2.4 V.

Potentials were post-*iR* corrected with resistance R_u determined by potentiostatic electrochemical impedance spectroscopy (EIS) after preconditioning at –0.8 V in the high-frequency region from 10^6 to 10^5 Hz at a phase angle of $\varphi = 0°$; amplitude was set to $\Delta E = 10$ mV.

2.2. Cyclic voltammetry at elevated pressure

For electrolysis at elevated pressure, a 316L stainless steel cell with a volume of 300 mL and a sapphire window for observation of the electrochemical experiments was used. Electrochemical measurements were carried out with a *Metrohm Autolab PGSTAT204* potentiostat. A detailed

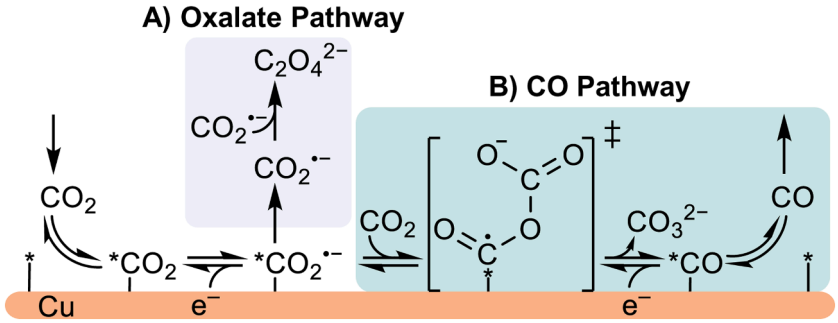

Fig. 1. Proposed mechanism for electrocatalytic CO_2 reduction on Cu in dry aprotic electrolytes with two competing reaction pathways: (A) towards oxalate formation and (B) towards carbon monoxide and carbonate formation. Asterisks (*) denote active Cu centers and adsorbed species at the electrode surface.

description, including a photograph and piping and instrumentation diagram (P&ID), are given in Puring et al. [50]

Inside the cell, a three-electrode setup consisting of an 8 cm^2 (4 · 2 cm^2) Cu foil (99.9999 %, *Thermo Scientific Chemicals*, unpolished as purchased), as working electrode, an $AgBF_4$-coated silver wire (in 0.1 mol L^{-1} $TBABF_4$ in acetonitrile) as quasi-reference and a platinum gauze (5 · 5 cm^2, Ø 0.1 mm Pt wire, 52 mesh) counter-electrode was used.

Before the experiment, the reactor was filled with 200 mL the electrolyte (0.1 M $TBABF_4$ in acetonitrile) and purged five times with CO_2 (until 6 atm) under constant stirring with a magnet-operated stirrer. Afterward, the reactor was filled with CO_2 until the desired absolute pressure of 5 bar, 10 bar, or 25 bar was reached and remained stable for a period of 20 min.

A preconditioning step consisting of 20 consecutive CV cycles at 100 mV s^{-1} was performed, followed by potentiostatic EIS to estimate the internal resistance for *iR* correction. Afterwards 5 CV cycles at each scan rate of 300 mV s^{-1}, 200 mV s^{-1}, 100 mV s^{-1}, 50 mV s^{-1} in descending order were collected. The potential range for cycling in each of the above steps at elevated pressure was set to –0.966 V and –2.566 V vs. Ag/$AgBF_4$ (0.1 mol L^{-1} $TBABF_4$ in acetonitrile), which corresponds to –0.8 V and –2.4 V vs. Ag/AgCl (KCl_{sat} in H_2O).

2.3. Preparation of Cu nanoparticle electrode

The Cu nanoparticle electrode (Cu-NP) was prepared via drop-casting onto a polished glassy carbon disk electrode ($A = 0.1963$ cm^2) in a PEEK shroud purchased from *PINE Research Instrumentation Inc*. The catalyst ink consisted of 2 mg CuO nanoparticles, 750 µL deionized water (>16 MΩ cm), 250 µL isopropanol, 8.58 µL Nafion 5 % dispersion (D-520, *VWR International, LLC*), and 1.2 µL of 1 M NaOH mixed via ultrasonication for 10 min. A total of 10 µL of the ink was drop cast onto the glassy carbon electrode in three steps (3 µL, 3 µL, and 4 µL). A uniform coating distribution was achieved by rotating the electrode at 300 rpm for 30 min under atmospheric conditions between each and after the final drop casting step to allow drying. Finally, in order to reduce the CuO nanoparticles to metallic Cu, the coated electrode was placed together with a Pt-wire as the anode in a PTFE cell containing 150 mL of 1 mol L^{-1} NaOH solution and cycled between potentials of –0.3 V and –1.5 V vs RHE for 12 cycles. Subsequently, the same protocol and setup as in Section 2.1 was used.

3. Computational details

3.1. Model approach and assumptions

In this section, the dynamic model is described in detail, accounting for the reactions at the electrode surface and the transport of species in the diffusion layer. Fig. 2 presents a schematic of the 1D model. The model parameters are listed in Table 1.

Our dynamic model considers the cathodic half-cell processes with a planar copper working electrode immersed in a stagnant acetonitrile electrolyte solution saturated with CO_2. At the surface of the working electrode, microkinetic sorption processes and electron transfer reactions occur. We have adopted the proposed mechanism by Amatore and Savéant (Fig. 1) with the following assumptions: [39]

(i) The electrolyte is water-free $c_{H_2O/H^+} = 0$.
(ii) Langmuir adsorption model applies to CO_2 and CO on Cu.
(iii) CO_2 initially undergoes adsorption prior to its reduction to the CO_2 radical anion.
(iv) The radical anion remains adsorbed on the surface, eliminating the oxalate pathway, as species analysis in the electrolyte by Ikeda and Figueiredo did not reveal any oxalate on Cu [23,36]. This further implies that the second electron transfer occurs heterogeneously from the electrode rather than from a radical anion in the liquid diffusion layer.
(v) CO/carbonate formation occurs via adsorbed $*CO_2^{\bullet-}$ and a second CO_2 from solution [31].
(vi) CO_2 attachment to the radical anion, subsequent electron transfer, and carbonate detachment are treated as a single reaction step, omitting the carbonic formic anhydride radical anion, which, to the best of our knowledge, has not been experimentally confirmed and is therefore considered by us to be a short-lived transition state.

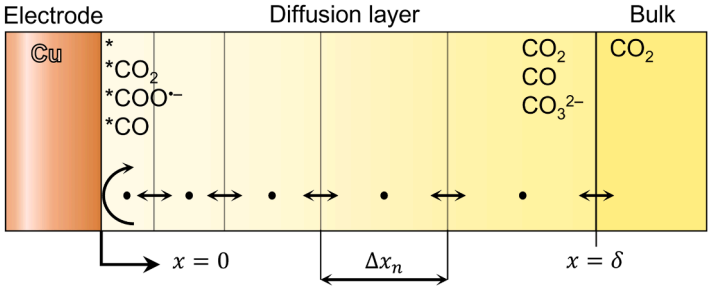

Fig. 2. Schematic of the model system. The reaction plane is located at the electrode-electrolyte interphase at $x = 0$. The end of the diffusion layer, at $x = \delta$, is the boundary to the bulk layer, for which a constant concentration is assumed.

Table 1
Model parameters for the planar Cu electrode.

Parameter	Symbol	Value	Unit	Source
Geometric surface area of electrode	A	$1.9635 \cdot 10^{-5}$	m^2	
Areal double layer capacitance	C_{dl}	0.831	F m^{-2}	experimentally determined
Uncompensated internal resistance	R_u	86	Ω	experimentally determined
Initial CO_2 concentration (for $p = 1.01325$ bar)	c_{0,CO_2}	0.278	mol L^{-1}	calculated from [42]
Henry solubility coefficient of CO_2 in acetonitrile	H^{cp}_{s,CO_2}	0.3113	mol L^{-1} bar	calculated from [42]
Binary liquid diffusion coefficient of CO_2 in acetonitrile	D_{CO_2}	$4.617 \cdot 10^{-9}$	m^2 s^{-1}	calculated from [51]
Binary liquid diffusion coefficient of CO in acetonitrile	D_{CO}	$5.043 \cdot 10^{-9}$	m^2 s^{-1}	calculated from [51]
Binary liquid diffusion coefficient of CO_3^{2-} in acetonitrile	$D_{CO_3^{2-}}$	$4.352 \cdot 10^{-9}$	m^2 s^{-1}	own estimation

(vii) Electrochemical reaction steps are considered only in the cathodic direction and are irreversible because only high cathodic potentials below –0.8 V are considered.

The above assumptions lead to the following mechanism, which consists of four steps: CO_2 adsorption (1), CO_2 reduction (2), CO formation (3), and CO desorption (4):

$$CO_2 + * \overset{r_{ads,CO_2}}{\rightleftharpoons} {}^*CO_2 \tag{1}$$

$${}^*CO_2 + e^- \overset{r_{red,CO_2}}{\rightarrow} {}^*CO_2^{\bullet -} \tag{2}$$

$${}^*CO_2^{\bullet -} + CO_2 + e^- \overset{r_{form,CO}}{\rightarrow} {}^*CO + CO_3^{2-} \tag{3}$$

$${}^*CO \overset{r_{des,CO}}{\rightleftharpoons} CO + * \tag{4}$$

Here, * denotes free adsorption sites or adsorbed species if followed by a chemical symbol, e.g., $*CO_2$. The rates of CO_2 adsorption, and CO desorption, are given by

$$r_{ads,CO_2} = \left(k_{ads,CO_2} \cdot a_{CO_2} \cdot \theta_* - k_{des,CO_2} \cdot \theta_{CO_2}\right) \cdot \Psi \tag{5}$$

$$r_{des,CO} = \left(k_{des,CO} \cdot \theta_{CO} - k_{ads,CO} \cdot a_{CO} \cdot \theta_{free}\right) \cdot \Psi \tag{6}$$

where θ_*, θ_{CO_2} and θ_{CO} are the coverage of the surface by free adsorption sites, CO_2, and CO respectively, a_{CO_2} and a_{CO} are the activities of CO_2 and CO in solution, k_{ads,CO_2}, k_{des,CO_2} and $k_{des,CO}$, $k_{ads,CO}$ are the rate constants for CO_2 and CO adsorption and desorption, respectively. Ψ refers to the roughness factor introduced in Section 4.3, which is set to 1 unless otherwise specified.

The rate equations of the electrochemical reactions, steps (2) and (3), are irreversible reactions using a Tafel-type kinetic, which relates the reaction rate to the potential E at the electrode-electrolyte interface,

$$r_{red,CO_2} = k_{red,CO_2} \cdot \theta_{CO_2} \cdot \exp\left(-\frac{(1-\alpha_{red,CO_2})FE}{RT}\right) \cdot \Psi \tag{7}$$

$$r_{form,CO} = k_{form,CO} \cdot \theta_{CO_2^{\bullet -}} \cdot a_{CO_2} \cdot \exp\left(-\frac{(1-\alpha_{form,CO})\mathrm{FE}}{\mathrm{RT}}\right) \cdot \Psi \tag{8}$$

with the surface coverage $\theta_{CO_2^{\bullet -}}$ of the radical anion, the charge transfer coefficients α_{red,CO_2} and $\alpha_{form,CO}$, and the cathodic rate constants k_{red,CO_2} and $k_{form,CO}$ for the respective reaction step, Faraday constant F, and RT, the product of temperature and universal gas constant. By assuming constant equilibrium potential E^0, we define the above electrochemical rate equations not in terms of the overpotential $\eta = E - E^0$, but directly in terms of E, while E^0 is contained inside the rate constant. The activities a of all species in the electrolyte solution are calculated from their dissolved concentrations and assume an ideal solution ($\gamma = 1$ and $c_{std} = 1$ mol L^{-1}). Changes in the coverage by species on the electrode surface are accounted for by the species balance

$$\frac{d\theta_{CO_2}}{dt} = \frac{1}{\Gamma} \cdot \left(r_{ads,CO_2} - r_{red,CO_2}\right) \tag{9}$$

$$\frac{d\theta_{CO_2^{\bullet -}}}{dt} = \frac{1}{\Gamma} \cdot \left(r_{red,CO_2} - r_{form,CO}\right) \tag{10}$$

$$\frac{d\theta_{CO}}{dt} = \frac{1}{\Gamma} \cdot \left(r_{form,CO} - r_{des,CO}\right) \tag{11}$$

$$\frac{d\theta_{free}}{dt} = \frac{1}{\Gamma} \cdot \left(r_{des,CO} - r_{ads,CO_2}\right) \tag{12}$$

with the areal concentration of adsorption sites Γ [47].

The consumption and production of species at the electrode give rise to a concentration gradient and a corresponding diffusion flux of species in solution, as described by Fick's law. As neither the solution was not stirred nor the electrode rotated, convection is neglected, and a thick diffusion layer can be assumed. This diffusion layer represents the model system boundaries. Assuming a planar electrode reduces this domain to one spatial dimension, x, normal to the working electrode surface (Fig. 2) [52]. The boundary at $x = 0$ corresponds to the reaction plane at the electrode-electrolyte interface. The other end of the domain, located at $x = \delta$, represents the boundary to the electrolyte bulk. The bulk phase is assumed to be permanently saturated with CO_2, whereas concentrations of CO and CO_3^{2-} are 0 and assumed to remain constant. The diffusion layer is discretized into 100 segments with logarithmically increasing width Δx_n, where n denotes the consecutive numbering of the segments. The total thickness of the diffusion layer δ is set to 6 mm, corresponding to the distance that a generated CO at the electrode can diffuse during a simulation time of 192 s, i.e., 3 cycles between −0.8 V and −2.4 V at a scan rate of 50 mV s^{-1} ($\delta \approx 6\sqrt{D_i t}$) [52]. This thickness ensures that arising concentration gradients are fully contained inside the model domain. Transport of carbonate by migration in the electric field is neglected by considering an excess of supporting electrolyte (0.1 mol L^{-1}) and only low production rates [53]. Additionally, we assume the supporting electrolyte to be inert within the potential window and an isothermal environment at ambient conditions (25 °C, 1.013 bar). At the initial state of the simulation, the $*CO_2$ surface coverage is in equilibrium with the liquid phase, which is homogeneously saturated with CO_2, whereas the concentrations of CO and carbonate are set to 0. The species balance for each species in the solution is then given by

$$\frac{\partial c_{CO_2,n}}{\partial t} = D_{CO_2} \frac{\partial^2 c_{CO_2,n}(x,t)}{\partial x^2} \tag{13}$$

$$\frac{\partial c_{CO,n}}{\partial t} = D_{CO} \frac{\partial^2 c_{CO,n}(x,t)}{\partial x^2} \tag{14}$$

$$\frac{\partial c_{CO_3^{2-},n}}{\partial t} = D_{CO_3^{2-}} \frac{\partial^2 c_{CO_3^{2-},n}(x,t)}{\partial x^2} \tag{15}$$

where D is the binary liquid diffusion coefficient of the dissolved species in the electrolyte. The diffusion coefficients of CO and CO_2, D_{CO} and D_{CO_2}, were estimated using Tyn and Calus method under the assumption of dilute solutions [51]. For the diffusion coefficient of carbonate, a linear relationship between the estimated diffusion coefficients of CO and CO_2 to their molar mass was assumed and extrapolated to CO_3^{2-}. The Eqs. (13)–(15) are implemented using a finite volume discretization scheme in a non-uniform mesh with exponentially increasing cell width Δx_n according to

$$\Delta x_n = \Delta x_1 \cdot w^n, \tag{16}$$

where n is the consecutive numbering of the cells, and w is a constant growth factor set to 1.076, which yields a width of the first volume Δx_1 of 0.3 µm. At the boundary of the diffusion layer and the electrode surface, $x = 0$, the spatial concentration gradient is set to zero. To account for changes in the concentrations of each species due to adsorption/desorption and reactions, a source term $\dot{S}$, is added for the first cell ($n = 1$) in Eqs. (13)–(15)

$$\dot{S}_{CO_2} = -\frac{r_{ads,CO_2} + r_{form,CO}}{\Delta x_1} \tag{17}$$

$$\dot{S}_{CO_3^{2-}} = \frac{r_{form,CO}}{\Delta x_1} \tag{18}$$

$$\dot{S}_{CO} = \frac{r_{des,CO}}{\Delta x_1} \tag{19}$$

No homogeneous chemical reactions elsewhere in the electrolyte are assumed.

The faradaic current density j_F from the CO_2 reduction step and CO formation is given by Faraday's law

$$j_F = F \cdot \left(r_{red,CO_2} + r_{form,CO}\right) \tag{20}$$

where F is the Faraday constant. The total current density of the simulation j is calculated via Ohm's law from the potential drop due to the uncompensated internal resistance R_u, which is determined via electrochemical impedance spectroscopy and the geometric electrode area A.

$$j = \frac{E_{ext} - E}{R_u \cdot A} \tag{21}$$

E_{ext} refers to the externally applied potential of the potentiostat, whereas E represents the potential at the electrode-electrolyte interface. Finally, the charge at the electrode surface is balanced by taking the accumulation of charge in the double layer, the incoming charge from the total current j, and the outgoing charge from the faradaic current j_F into account:

$$\frac{dq}{dt} = \Psi \cdot C_{dl,planar} \cdot \frac{dE}{dt} = j - j_F \tag{22}$$

Here $C_{dl,planar}$ is the areal double layer capacitance of the polished planar Cu electrode.

The presented model is used to simulate cyclic voltammetry experiments, where the externally applied potential E_{ext} changes linearly with time by the scan rate v according to

$$E_{ext}(t) = \begin{cases} E_{ext}(t=0) - vt, & \forall\ t < t_s \\ E_{ext}(t=t_s) + vt, & \forall\ t \geq t_s \end{cases} \tag{23}$$

Sweeping from the high to low potential, at the switching time t_s, the direction of the linear sweep is reversed in opposite direction, marking the end of the negative-going sweep, denoted as the forward and the beginning of the positive-going, backward sweep.

3.2. Model implementation

The model is implemented and simulated with the MATLAB 2022b software. The set of differential equations was solved using the ode15 ODE solver function. High accuracy of the results is ensured by setting the absolute error tolerance to 10^{-12} and the maximum step size to 0.01 s.

3.3. Parameter identification

Kinetic parameters k_{ads,CO_2}, k_{des,CO_2}, k_{red,CO_2}, $k_{form,CO}$, $k_{des,CO}$, $k_{ads,CO}$, α_{red,CO_2}, $\alpha_{form,CO}$ and Γ of the model were identified from the cyclic voltammetry experiments shown in Fig. D.1b by mathematical parameter optimization. For each individual scan rate, the root mean squared error (RMSE) of the 3rd cycle between the experimental and simulated cyclic voltammograms was calculated by

$$\mathrm{RMSE} = \sqrt{\frac{\sum_{n=1}^{N}\left(j_{sim} - j_{exp}\right)^2}{N}} \tag{24}$$

where N is the number of data points, j_{sim} and j_{exp} are the corresponding simulated and experimental values of the current density at each data point during the 3rd CV cycle. The objective function was defined as the mean RMSE value of all scan rates. The particle swarm optimization algorithm built into MATLAB was used. It was restarted 100 times for 18,000 iterations each or until the convergence criteria (change in RMSE between iterations below 10^{-6}) was met. Each run consisted of 90 particles initialized at random starting values, resulting in a maximum number of evaluated parameter sets of $1.62 \cdot 10^8$. The simulation results with the best parameter set match the experimental data exceptionally well with an RMSE value of 0.1046 mA cm^{-2}.

The charge transfer coefficients α_{red,CO_2} and $\alpha_{form,CO}$ estimated in this study show a significant deviation from the symmetrical value of 0.5. As α represents the anodic charge transfer coefficient, the corresponding cathodic charge transfer coefficient $(1-\alpha)$ is relatively small. This is in good agreement with the electrode kinetic model by Butler-Volmer, which expects smaller values of the charge transfer coefficient in the electron-transfer enhancing rate for specifically adsorbed reactants, such as $*CO_2$ and $CO_2^{\bullet-}$, due to their closer proximity to the electrode surface plane [54].

The areal concentration of adsorption sites, Γ, corresponds to approximately 39 active sites per Cu atom of a perfectly flat single atom layer Cu(100) surface of the same dimensions. Such reference surface is purely theoretical. In reality, our Cu surface, even though it was thoroughly polished, is polycrystalline and cannot be assumed to be ideally flat with a substantially higher number of active sites due to unevenness and the presence of defects and grain boundaries.

4. Results and discussion

In the following section, we first report experimental cyclic voltammetry results from which we quantify the kinetic model parameters [46,55,49]. Subsequently, we conduct a comprehensive model-assisted analysis to identify the limiting processes. Lastly, operating and design measures are evaluated to optimize the CO_2R performance.

4.1. Characterization of CO_2R via cyclic voltammetry

Cyclic voltammetry was performed on a polished polycrystalline Cu electrode in a stagnant CO_2-saturated 0.1 M tetrabutylammonium tetrafluoroborate ($TBABF_4$) acetonitrile electrolyte. The experimental CVs for scan rates of 50 mV s^{-1}, 100 mV s^{-1}, and 200 mV s^{-1} are shown as dashed lines in Fig. 3a–c. The solid lines give the corresponding simulated CVs.

The experimental CVs exhibit a similar profile for all three scan rates. For potentials more positive than –1.4 V, the profiles are indistinguishable. At −1.4 V during the forward sweep, a cathodic current arises with an exponential slope for all scan rates. This slope starts to level off later with increasing scan rate: −2.0 V vs. −2.2 V for 50 mV s^{-1} and 200 mV s^{-1}, respectively. In addition, the maximum current density decreases by 23 %, from –1.93 mA cm^{-2} to –2.52 mA cm^{-2}. As the slope of the current density decreases at cathodic potentials beyond –2.0 V and higher cathodic peak current densities are obtained for faster scan rates, a limitation of the CO_2R is imminent. Here, the exponential slope becomes asymptotic for slow scan rates, suggesting a possible transport limitation. The backward sweep shows a rapid decline first, followed by a relatively linear and exponential slope, all at slightly lower current densities than the forward scan.

As experiments without CO_2 yielded no current in the potential range of –0.8 V to –2 V, see Fig. D.1a, we propose that the observed current can be attributed to CO_2 reduction. The onset potential in acetonitrile electrolyte is approximately 500 mV higher compared to similar voltammograms recorded in aqueous $KHCO_3$ electrolyte [56]. This is attributed to two reasons: (i) the absence of protons which are thought to facilitate the reduction through a proton-coupled-electron-transfer to *COOH [36], or to stabilize the radical-anion via hydrogen bonding [57], and (ii) the presence of tetraalkylammonium salt which is reported to sharply increase the overpotential of CO_2R even in aqueous solution [58].

Both, the high onset potential and the emerging limitations, need to be understood and addressed to increase the performance of CO_2R in aprotic electrolytes.

For this purpose, the kinetic model (see Section 3.1) is employed to simulate CVs at scan rates of 50 mV s^{-1} to 200 mV s^{-1}. The simulated CVs in Fig. 3 are in good agreement with the experiments for all scan rates.

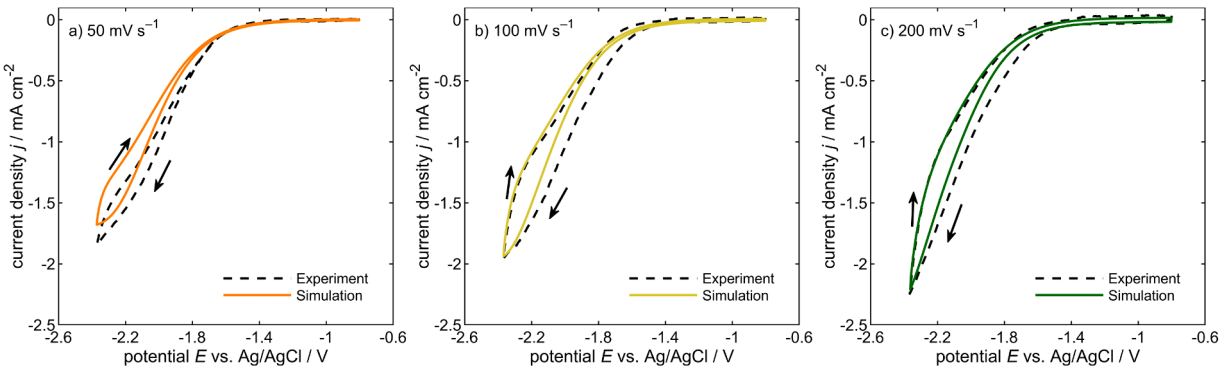

Fig. 3. Simulated (solid line) and experimental (dashed line) cyclic voltammograms for planar Cu electrode in 0.1 mol L^{-1} $TBABF_4$ in acetonitrile under CO_2 atmosphere at scan rates of (a) 50 mV s^{-1}, (b) 100 mV s^{-1} and (c) 200 mV s^{-1}; the *i*R-corrected third cycle is given vs. Ag/AgCl (KCl_{sat} in H_2O); potential limits are chosen to avoid Cu and electrolyte degradation.

Table 2
Kinetic parameter values identified via algorithm-based parameter optimization from cyclic voltammetry experiments.

Parameter	Symbol	Value	Unit
Charge transfer coefficient of CO_2 reduction	α_{red,CO_2}	0.8261	–
Charge transfer coefficient of CO formation	$\alpha_{form,CO}$	0.8700	–
CO_2 adsorption rate constant	k_{ads,CO_2}	$3.7899 \cdot 10^{-4}$	mol s^{-1} m^{-2}
CO_2 desorption rate constant	k_{des,CO_2}	$2.7887 \cdot 10^{-3}$	mol s^{-1} m^{-2}
CO_2 reduction rate constant	k_{red,CO_2}	$4.3524 \cdot 10^{-9}$	mol s^{-1} m^{-2}
CO formation rate constant	$k_{form,CO}$	$2.5494 \cdot 10^{-8}$	mol s^{-1} m^{-2}
CO desorption rate constant	$k_{des,CO}$	$8.2482 \cdot 10^{-4}$	mol s^{-1} m^{-2}
CO adsorption rate constant	$k_{ads,CO}$	$3.2463 \cdot 10^{-14}$	mol s^{-1} m^{-2}
Areal concentration of adsorption sites	Γ	$9.9949 \cdot 10^{-4}$	mol m^{-2}

Thus, the model with the identified parameter set (Table 2) is assumed to be a sound representation of the processes at the electrode, and it is used to give insight into processes and states at the electrode.

4.2. What limits CO_2 reduction?

The CV simulation at 100 mV s^{-1} is used to gain an in-depth insight into the evolution of reaction and transport rates during a CV and to identify which process causes limitations. Simulation results at scan rates of 50 mV s^{-1} and 200 mV s^{-1} lead to the same conclusions; details can be found in appendix B.

Fig. 4 depicts the rates of the four surface steps, the surface coverages of the species, and the concentration of CO_2 and CO at the electrode as a function of the cycled potential during the third CV cycle.

The CO_2 adsorption and CO_2 reduction rates in Fig. 4 share a similar profile with an exponential slope from –0.8 V to –1.9 V, after which both processes decelerate. Their rates during the backward sweep are almost identical to that of the forward sweep. CO formation initiates at a comparable potential, initially with a slower increase before accelerating and ultimately surpassing the preceding steps by 75 % towards the end of the forward sweep. Throughout the backward sweep, the rate of CO formation undergoes a rapid decline. Lastly, the process of CO desorption lags behind its production, exhibiting a discernible exponential surge at slightly lower potentials, once again surpassing the CO_2 adsorption and CO_2 reduction rates but reaching a 20 % lower rate than CO formation. During the backward sweep, this increase persists briefly before rapidly declining with the CO formation rate.

All rates, except the CO desorption rate, exhibit a slowdown below –2.2 V, indicating a limitation in the CO_2 reduction reaction in this potential region. Such limitation arises from a limiting reaction step or the restricted availability of a reactant caused by either slow mass transport or adsorption. Here, the surface coverages must be considered.

Fig. 4b presents the surface coverages θ by free sites (*) or by the adsorbates *CO_2, *$CO_2^{\bullet-}$, and *CO. The coverage of free sites θ_* is

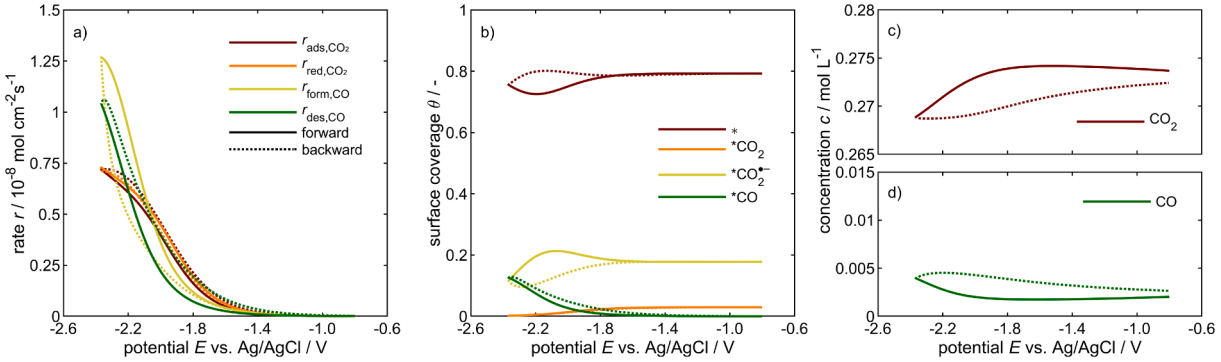

Fig. 4. Predicted changes of species and processes during a CV: (a) reaction rates, (b) surface coverages, (c) CO_2 concentrations and (d) CO concentration at the electrode-electrolyte interface. The solid line represents the forward, and the dotted line represents the backward sweep. The third CV cycle is shown for 100 mV s^{-1} scan rate.

continuously high, above 72 %, showing a minimum, and – on the backward sweep – a maximum around –2.2 V. The coverage of adsorbed CO_2 constantly remains at a low value, below 3 %. Below –1.4 V, it gradually decreases to a minimum of 0.18 % at the reversal point and returns to its initial values during the backward sweep. As a result, there is a deficiency of surface adsorbed CO_2, particularly at potentials below −2.0 V, which hampers the subsequent electrochemical reactions and, thus, compromises the overall CO_2 reduction performance. This can also be seen by the reaction rates: the CO_2 reduction step, which requires $*CO_2$ as a reactant, is under the control of the CO_2 adsorption and exhibits a slow rate with a similar profile to the CO_2 adsorption rate. Interestingly, the CO_2 adsorption rate demonstrates minimal hysteresis. This suggests rapid equilibration rather than slow kinetics, thus highlighting a thermodynamic limitation, i.e., the adsorption equilibrium favors the desorbed state for CO_2.

The coverage of $CO_2^{\bullet-}$ significantly drops to 9 % in the potential region of low CO_2 coverage, whereas at less cathodic potentials, it remains at around 18 % coverage. Overall, the profile of the $CO_2^{\bullet-}$ coverage is characterized by a significant hysteresis between –1.7 V and –2.3 V. $CO_2^{\bullet-}$ coverage increases below −1.4 V as the electroreduction of adsorbed CO_2 starts to occur. At –2.0 V, when CO formation kicks in, $CO_2^{\bullet-}$ coverage increase slows down and transitions into a decrease before gradually returning to its initial state during the backward sweep. There is no coverage by CO initially. Below −1.4 V, it gradually increases to 12 % as *CO is produced more rapidly than it desorbs.

We note significant limitations from the surface coverages with less than a third of the catalyst's active sites engaged in CO_2 conversion, indicating a substantial optimization opportunity. We propose two explanations for this phenomenon. Firstly, the adsorption equilibrium at ambient conditions appears to be thermodynamically unfavorable, resulting in a low CO_2 coverage. Secondly, in our simulations, all active Cu sites are equally likely to adsorb CO_2, whereas, in reality, undercoordinated sites exhibit significantly higher activity for CO_2 adsorption [59]. A possible blockage of adsorbed salt on the electrode has not been reported for the here used $TBABF_4$ [29].

To analyze a possible transport effect of the reactant CO_2 and the product CO, their local concentration at the electrode-electrolyte interface is shown in Fig. 4c and d. The CO_2 concentration is at a constantly high value near the saturation limit of 0.278 mol L^{-1}, exhibiting only a marginal decrease of 2 % at –2.3 V. During the backward sweep, the CO_2 concentration gradually recovers but settles at a slightly lower concentration compared to the start of the CV cycle. This gap gradually decreases over the subsequent cycles. The current density also slightly shifts to higher values due to this lower concentration at the start of each cycle. In combination, this indicates that in aprotic electrolytes, CO_2R is impeded not only by CO_2 adsorption, but also by CO_2 transport. However, the impact of transport here is small as the CO_2 concentration remains at overall high levels. Thus, CO_2 transport does not impose a limitation on the reaction during dynamic potential cycling.

The CO concentration, Fig. 4d, maintains low values, reaching a maximum of 5 mmol L^{-1} during the most rapid CO production. This minimal increase indicates that transport is not a limiting factor here either. Further, operation at 50 % of the scan rate shows no impact on the CO_2 adsorption and reaction rate. Consequently, concerns about transport limitations in acetonitrile can be dismissed for the given scan rates down to 50 mV s^{-1} at a flat Cu electrode.

In order to verify our claim of a CO_2 adsorption limitation and only minor effects of CO_2 transport under more practically relevant stationary operation, we simulated a polarization curve, shown in Fig. 5, and compared the resulting current density, CO_2 coverage, and CO_2 concentration at the electrode-electrolyte interface to those of the dynamic CV.

The stationary current density in Fig. 5a exhibits a profile similar to that of the dynamic CV at 100 mV s^{-1}. A notable cathodic current starts at –1.4 V with an increasing slope until –2.0 V, where the slope

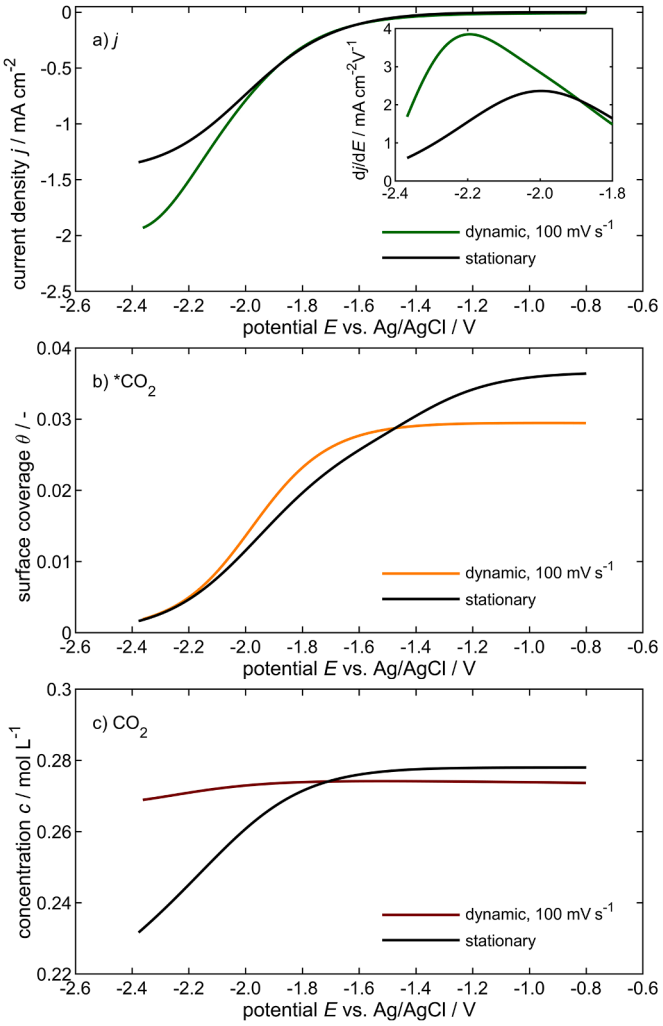

Fig. 5. Comparison of simulated cathodic polarization curve (stationary) and forward sweep of the 3rd CV cycle with a scan rate of 100 mV s^{-1} (dynamic): (a) current density and derivative of current density with respect to potential dj/dE, (b) CO_2 coverage and (c) CO_2 concentration at the electrode-electrolyte interface.

decreases, indicating the beginning of the performance-limited region. In comparison, the slope of the dynamic CV continues to increase until –2.2 V before a limitation is evident. The derivatives of the current density dj/dE, shown in the inset of Fig. 5a, further illustrate the limiting potential region below –2.0 V for stationary operation and below –2.2 V for the dynamic case.

The CO_2 coverage and the CO_2 concentration in Fig. 5b and c, respectively, exhibit a monotonous decrease in the stationary case. Additionally, the CO_2 coverage of the stationary case is at higher levels for potentials above –1.5 V, presumably because it has more time to equilibrate, but starts to decrease at higher potentials. Ultimately, both curves converge to a low CO_2 coverage of 0.2 % at –2.3 V. Similarly, the CO_2 concentration for the stationary case is higher at potentials above –1.7 V. It decreases at lower potentials in both cases, stationary and dynamic. While this decrease is significantly more pronounced for the stationary case, the CO_2 concentration shows no sign of depletion during either operation. The remaining stationary CO_2 concentration at –2.3 V is 83 % of the maximum solubility, compared to 97 % during the dynamic CV. While both operation modes suffer from a substantial adsorption limitation, the performance disparity between stationary and dynamic operation can be attributed to transport effects, i.e., differences in the local CO_2 concentration at the electrode-electrolyte interface.

During dynamic potential cycling, the reactions halt above −1.4 V (Fig. 4a), and the CO_2 concentration essentially recovers via diffusion of CO_2. In contrast, during stationary operation, CO_2 is consumed faster than it is transported, leading to lower concentrations at the electrode-electrolyte interface and thus resulting in lower current density.

In summary, the depletion and insufficient CO_2 coverage below −2.0 V, even though a high CO_2 concentration in solution is present in both dynamic and stationary operation, is evidence that the CO_2 adsorption is the primary limiting, i.e., rate-determining reaction step. The subsequent reaction steps are inhibited because the rate at which their reactants are supplied is insufficient. This conclusion challenges the widespread assumption that the radical anion formation is rate-determining in aprotic electrolytes [37], a presumption we attribute to the tendency to view CO_2 adsorption and the electron transfer as unified step. Our dynamic analysis separates these steps and allows them to be distinguished kinetically. Note that stationary analysis would not allow separation of the rates, as all reaction rates would be equal. Our finding of CO_2 adsorption limitation at high conversion rates agrees with Gauthier, reporting that electron transfers at metal–solution interfaces are generally fast and unlikely to be rate-determining [60]. Furthermore, our findings about CO_2 reduction in aprotic electrolytes are in contrast to aqueous electrolytes, where kinetic modeling of CO_2R in $KHCO_3$ electrolyte by our group identified the slow transport of CO_2 as the main bottleneck [47].

4.3. How to improve performance?

The previous sections show that CO_2 adsorption is the bottleneck of the electrochemical CO_2 reduction process in acetonitrile. Therefore, it is necessary to focus on overcoming this adsorption limitation to achieve performance improvements. Sensitivity analysis of kinetic, geometric, and operational parameters on the performance was conducted (see appendix A). The activity-area-related parameters, surface roughness and concentration of adsorption sites, and the operational parameter, pressure, showed significant impact.

The concentration of adsorption sites is inherent to the catalyst material, describing the number of active sites per surface area of the electrocatalyst in our model, which in practice cannot easily be changed without altering the catalytic activity. On the other hand, surface roughness is a geometrical parameter that can be modified in technical systems [61]. Thus, in the following section, we focus on the two parameters, surface roughness and pressure, and make model-based predictions to analyze their impact on enhancing CO_2R performance, followed by experimental verification.

The roughness of an electrode is a crucial factor in electrocatalysis as it creates more undercoordinated sites on the electrode surface, which are highly active and, thus, improve the performance of the electrode [62]. Here, roughness is quantified as the roughness factor Ψ, defined as the ratio of electrochemical surface area (ECSA) relative to the geometric area of an electrode. Assuming proportionality between the double layer capacitance and the ECSA, the roughness factor of an electrode can be estimated as the ratio of the measured double layer capacitance relative to that of a flat polycrystalline Cu electrode (see appendix C Section 4). This flat Cu electrode with Ψ set to 1, has been used in the previous sections. Note that this does not mean that the electrode is ideally flat but instead provides a practical reference to quantify an increase in ECSA due to surface modification. This definition allows our predictions to be transferable to porous, particle-based electrodes, where ECSA can be influenced by changing particle size and loading or surface morphology until transport-constraining effects become relevant [63].

To account for surface roughness changes in our model, all reaction rates and the areal double layer capacitance, which are linearly dependent on the active surface area, are multiplied by Ψ. The simulated CVs and corresponding CO_2 coverages and CO_2 concentrations for $\Psi = 1$ (reference), 2, 5, and 10 are given in Fig. 6.

According to the simulations, an increase in the roughness factor leads to an increase in cathodic current density. The simulated CVs exhibit a similar shape for all values of Ψ: no observable current at high potentials and a transition into exponential growth at low potentials. The onset of this growth occurs at less negative potentials and exhibits a steeper slope for higher roughness values, resulting in higher maximum current densities. There is a small hysteresis in all cases, as the current density during the backward sweep follows a similar profile but at slightly lower levels.

The initial CO_2 coverage shown in Fig. 6b is slightly lower for higher values of Ψ. However, the overall profile is similar: At potentials below −1.4 V, the CO_2 coverages decrease similarly for all shown roughness values and reach the same minimum. The differences in initial coverage can be explained by the CO_2 concentration at the electrode (Fig. 6c). Due to the higher consumption rate of CO_2 with increased surface roughness, the concentration decreases more substantially. Additionally, the difference between the CO_2 concentration at the start and end of each cycle increases as the higher CO_2 consumption rate at the electrode is not balanced by the slow diffusional transport of CO_2 to the electrode, indicating a small transport effect. However, the CO_2 concentration remains above 70 % of the saturation limit even at the lowest potentials. Hence, we dismiss a limiting transport effect on the performance, even with a tenfold increased surface area. Instead, as the potential becomes more negative, the CO_2 coverages decrease similarly for all shown roughness values and converge to the same minimum below –2.2 V due to unfavorable CO_2 adsorption equilibrium. Therefore, we conclude that CO_2 adsorption remains the main limitation. The increase in current density at higher Ψ originates from the larger active surface area available for surface processes, including CO_2 adsorption.

To confirm these model-based predictions of the performance improvement by higher surface roughness, we performed experimental CV measurements using a Cu nanoparticle-coated electrode (Cu-NP), shown in Fig. 6d. The roughness of the Cu-NP electrode was estimated to be 1.7 with the flat Cu electrode as reference, which agrees with the

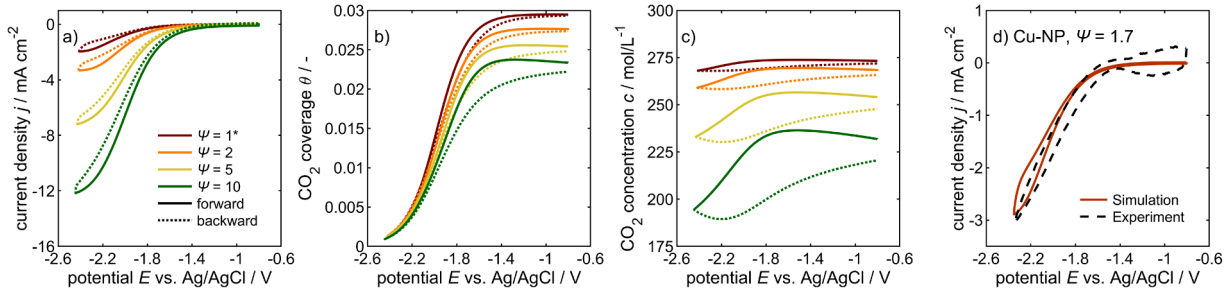

Fig. 6. Impact of surface roughness on CO_2R performance: (a) Simulated cyclic voltammograms with a scan rate of 100 mV s^{-1} for roughness factors Ψ from 1 to 10 (* $\Psi = 1$ corresponds to the dynamic results from the previous section). (b) the corresponding CO_2 coverage and (c) CO_2 concentration at the electrode-electrolyte interface. (d) Comparison of experimental and simulated CV for the Cu-NP electrode with an $\Psi = 1.7$.

reported value for in situ generated Cu spheres [64]. Further information on the roughness factor determination can be found in appendix C (Figs. C.1 and C.2).

The experimental CV for the Cu-NP electrode exhibits a peak current density of 150 % that of the polished Cu electrode, which is in good agreement with the simulations using the same roughness factor of the Cu-NP electrode, thus confirming the model predictions. There is a notable difference between the simulation and the experimental CV of the Cu-NP electrode at potentials above −1.4 V. The Cu-NP electrode exhibits a strong capacitive-like hysteresis in this region, which our model cannot reproduce. We hypothesize that this behavior may be attributed to the swelling of the Nafion ionomer binder used to immobilize the Cu nanoparticles on the glassy carbon substrate upon exposure to acetonitrile electrolyte [65]. Additionally, the slightly porous morphology of the drop casted electrode may contribute to this phenomenon as well [66].

Fig. 8a shows a relatively linear dependence of the current density at −2 V (100 mV s^{-1}) on the roughness below $\Psi < 10$. For higher roughness, the current increases less strong, as transport plays an increasingly important role. However, a transport limitation, i.e., a depletion of CO_2 at the electrode-electrolyte interface, is only expected at unrealistic high roughness factors > 500. Thus, porous electrodes for CO_2 reduction in acetonitrile are a feasible way of reaching higher current densities without significant transport limitations.

Next, we will elucidate the other performance-sensitive parameter: pressure. The underlying reason for the pressure sensitivity is the CO_2 adsorption equilibrium: With increasing pressure, the CO_2 concentration in the electrolyte solution increases, and in turn, the CO_2 adsorption equilibrium shifts towards higher CO_2 coverages. In the following, we present model-based predictions and in-depth analysis of the effect of pressure up to 40 bar on CO_2R performance and its limitation to enhance CO_2 adsorption, to pave the way for tailored operational and design measures to improve CO_2R performance.

The effect of pressure on the CO_2 solubility in acetonitrile over the entire pressure range is modeled by Henry's law assuming ideal solution, i.e., CO_2 solubility increases linearly with pressure. Recent studies have reported a more complex relationship, suggesting that the solubility of CO_2 in acetonitrile-based electrolytes follow an exponential trend rather than a linear one [67–69]. It is important to note this simplification may introduce some limitations to the accuracy of our modeling approach at elevated pressure. Nevertheless, the obtained trends are qualitatively valid and contribute valuable insights to the understanding of CO_2 reduction kinetics under elevated pressure conditions.

Fig. 7 presents the simulated CVs and corresponding CO_2 coverage for absolute pressures of 1 bar, 2 bar, 5 bar, and 10 bar.

The simulated CVs in Fig. 7a show a consistent pattern for all four pressures, with initially flat profiles during the forward sweep, followed by an exponential growth of cathodic current. The onset of this increase is shifted to less negative potentials for higher pressures and exhibits a steeper slope. In addition, the maximum current densities obtained at −2.4 V are significantly higher at elevated pressures. The impact of pressure on the CV closely resembles that of higher surface roughness. In contrast, pressure has a much more substantial impact on CO_2 coverage, as seen in Fig. 7b: the initial CO_2 coverage increases significantly with higher pressure, from 2.8 % at 1 bar to 25 % at 10 bar. However, as the potential is swept in the cathodic direction, the CO_2 coverage significantly decreases for all pressures, reaching low values close to zero around –2.2 V. During the backward sweep, CO_2 coverage builds up again in a similar profile, including a small hysteresis.

According to the model predictions, increasing pressure leads to significantly higher peak current densities and higher CO_2 coverages, and thus CO_2 reduction performance. However, similarly to the surface area increase, the CO_2 coverage decreases sharply during the forward sweep at all pressures and therefore still limits CO_2 reduction performance.

Experimental CVs over a wide pressure range from 0.11 bar to 25 bar were subsequently performed to validate the model predictions. For experiments below 1.013 bar, the CO_2 partial pressure was precisely controlled by blending the incoming CO_2 feed with inert argon gas in varying compositions using the same cell as in the previous sections. For pressures exceeding 1.013 bar, a gas-tight pressurized cell was utilized as described elsewhere [50,70]. It is possible that the kinetic parameters of our model obtained from the ambient pressure cell may introduce additional uncertainties into our simulations of the high-pressure cell, considering the substantial differences in their respective designs and scales.

Fig. 8b and c compare the experimental and simulated current densities at −2.0 V during a CV for the subatmospheric and high-pressure range. The complete CVs as well as additional parameters for the simulations at elevated pressure are given in Figs. D.2 and D.3 and Table D.1 of the Appendix. A roughly linear correlation between current density and pressure emerges within the subatmospheric pressure range. While our simulations accurately replicate this trend, the experimentally obtained current density fall partly below the predicted values.

In the high-pressure range, the simulations demonstrate an asymptotic trend rather than a linear one, approaching near-flat behavior at 40 bar. We attribute this to the increased coverage of adsorption sites by CO_2 at higher pressures, rendering any further increase in pressure less effective. Once again, our model successfully captures the nonlinear pressure-performance relation but shows some deviation. The experiment shows an earlier saturation of the pressure impact, already before 25 bar. This can be attributed to the limited applicability of Henry's Law for CO_2 solubility at elevated pressures [67–69], as well as the substantial differences in designs and scales between the high pressure and ambient pressure setup. Notably, the experimental CVs at elevated pressure depicted in Fig. D.3 also exhibit a deviation from our simulations, failing to clearly indicate a limitation at high cathodic potentials, in contrast to what the model predicts. We attribute this discrepancy to

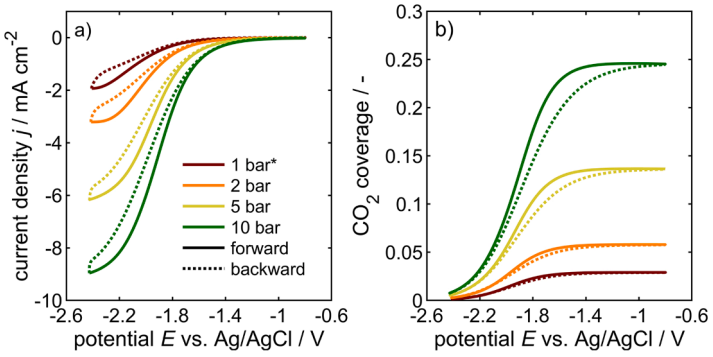

Fig. 7. Impact of pressure on CO_2R performance: (a) Simulated cyclic voltammograms with a scan rate of 100 mV s^{-1} for absolute pressures from 1 bar to 10 bar, and (b) the corresponding CO_2 coverages (* p = 1 bar corresponds to the dynamic results from the previous section).

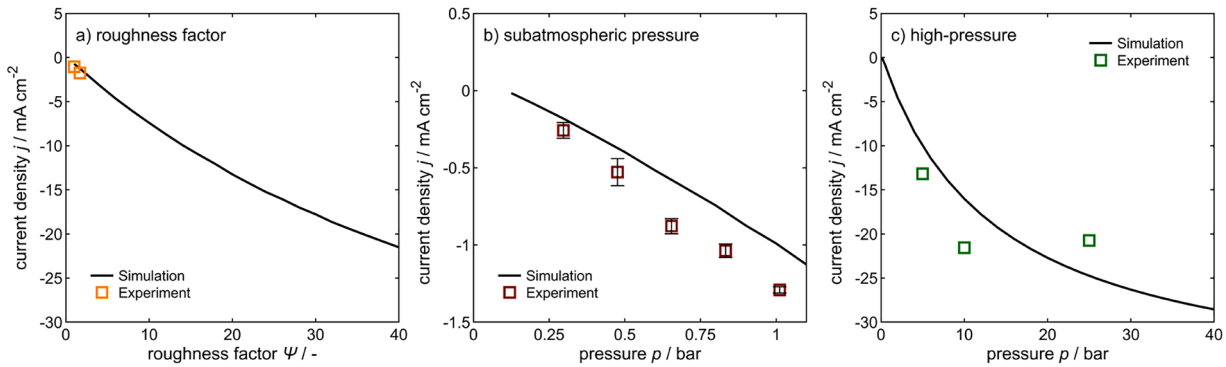

Fig. 8. Impact of roughness factor and pressure on current density at −2.0 V during a CV with a scan rate of 100 mV s^{-1}. (a) Simulation of roughness factors up to 40 and Cu-NP experiment with an estimated roughness factor of 1.7. (b) Simulation and experiments of subatmospheric pressure CVs ($\leq$ 1.013 bar, $\Psi = 1.4$) and (c) high-pressure CVs up to 40 bar with a Cu foil ($\Psi = 2.8244$).

the aforementioned factors, although based on our model we cannot exclude other contributing factors, such as alterations in heterogeneous charge transfer kinetics, or changes in CO_2 diffusivity due to decreased viscosity of the liquid electrolyte caused by volumetric expansion upon pressurization with CO_2 [67].

In summary, the model-based predictions of the surface roughness show that increasing roughness factor improves the performance of the CO_2R process but does not resolve the adsorption limitation imposed by the unfavorable thermodynamic equilibrium. Instead, the increase is solely due to the larger active surface area. Therefore, especially in organic electrolytes with high CO_2 solubility, high surface area electrodes are an effective means to improve CO_2R performance. The simulations and experiments at varying pressures show that increasing the pressure up to 10 bar can improve the performance despite the adsorption limitation. The higher initial CO_2 coverage at elevated pressure can mitigate the unfavorable thermodynamic equilibrium of CO_2 adsorption, resulting in significant performance improvements. Consequently, raising pressure represents another viable strategy to boost CO_2 reduction performance. A similar increase in performance can be expected from solvents with even higher CO_2 solubility, provided their electrochemical stability at relevant cathodic potentials.

5. Conclusions

This work presented the first dynamic reaction-transport model for electrochemical CO_2 reduction in aprotic electrolytes. The experimentally validated model provided a quantitative understanding of the surface processes, concentration profiles, and surface coverages during dynamic operation for Cu electrodes at different operating conditions. Kinetic parameters were derived from experimental cyclic voltammograms. Analysis revealed for all conditions the same performance limitation in acetonitrile electrolyte: the adsorption of CO_2 on Cu is the kinetic bottleneck, i.e., the rate-determining step, as opposed to the limiting transport of CO_2 in aqueous solution [47]. Furthermore, our findings challenge the widely-held belief that the formation of the CO_2 radical anion is rate-determining in aprotic systems on Cu and highlight the importance of improving CO_2 adsorption in the overall reaction process.

To understand how to improve CO_2 reduction and to see if another step becomes limiting under different conditions, we systematically varied operating conditions, such as pressure and scan rate, as well as electrode design, via roughness and, thus, active surface area. Our results show that higher electrode roughness and pressure significantly improve the CO_2R performance by increasing the active surface area or the surface coverage of CO_2, respectively. Despite the performance improvements, CO_2 adsorption remains the bottleneck under all studied conditions. We note that our conclusion at elevated pressure may be subject to additional factors and limitations from our linear approximation of the CO_2 solubility. The difficulty in overcoming the adsorption limitation emphasizes the critical role of this step in the CO_2 reduction process. It highlights the need for additional solutions to improve the reactant's adsorption rate and the electrocatalyst's adsorption capability, e.g., by catalyst or electrolyte design.

The model-based approach presented here is simple and widely adaptable. Using CO_2R on Cu as a model system, we established a foundation for the model-based kinetic analysis and the model-assisted design of process and operating parameters in organic electrolytes. It may serve as a basis for the modeling of other CO_2R electrocatalysts or more complex electro-organic reaction systems. Overall, our study paves the way for further model-assisted investigations to improve the performance and sustainability of CO_2 reduction to valuable chemicals in unconventional electrolytes.

CRediT authorship contribution statement

Niklas Oppel: Writing – original draft, Validation, Software, Methodology, Investigation, Formal analysis, Data curation. **Philipp Röse:** Writing – review & editing, Supervision, Resources, Project administration, Conceptualization. **Stephan Heuser:** Writing – review & editing, Investigation. **Michael Prokein:** Writing – review & editing, Resources. **Ulf-Peter Apfel:** Writing – review & editing, Resources. **Ulrike Krewer:** Writing – review & editing, Supervision, Project administration, Funding acquisition, Conceptualization.

Declaration of competing interest

The authors declare that they have no known competing financial interests or personal relationships that could have appeared to influence the work reported in this paper.

Data availability

The data presented in the manuscript are openly available in the KITopen repository at: https://doi.org/10.35097/1853.

Acknowledgments

We express our sincere gratitude to Kathrin Riemann for her assistance in the experimental investigation. Additionally, our appreciation goes to Dr. Steffen Czioska, formerly associated with the Institute for Chemical Technology and Polymer Chemistry (ITCP) at the Karlsruhe Institute of Technology, for generously providing us with copper nanoparticles. Open Access funding enabled and organized by Projekt DEAL.

Appendix A. Parameter Sensitivities

Local parameter sensitivity analysis was performed to investigate which model parameters have the most significant impact on the CO_2R performance. The target quantity was the simulated cathodic current density j at −2.3 V. It was determined how much it changes in response to ±10 % change in a single parameter.

The following parameters were investigated: rate constants (k_{ads,CO_2}, k_{des,CO_2}, k_{red,CO_2}, $k_{form,CO}$, $k_{des,CO}$, $k_{ads,CO}$), charge transfer coefficients (k_{red,CO_2} and $\alpha_{form,CO}$), adsorption site density Γ, scan rate ν, surface roughness factor Ψ, and absolute pressure p.

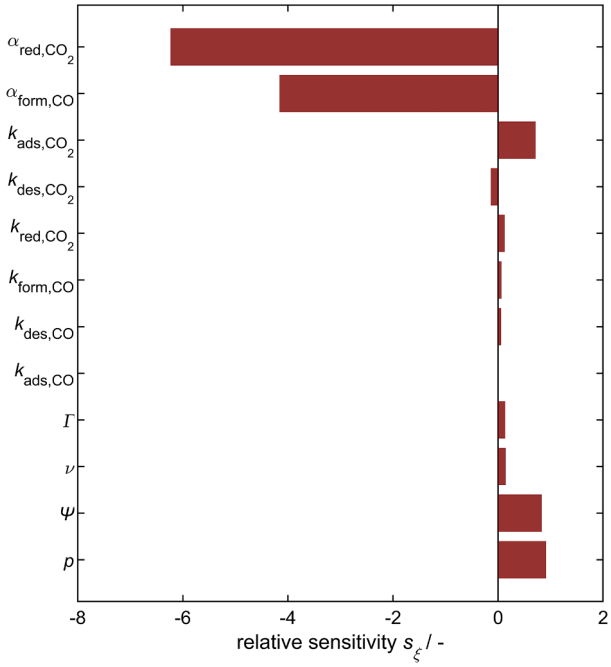

Fig. A.1. Relative sensitivity of the model parameters on simulated current density at −2.3 V, calculated by varying each parameter by ±10 %.

For each parameter ξ, the relative sensitivity denoted as s_ξ was determined (Fig. A.1) according to

$$s_\xi = \frac{f(\xi_0 + \Delta\xi) - f(\xi_0 - \Delta\xi)}{2\Delta\xi} \cdot \frac{\xi_0}{f(\xi_0)} \tag{A.1}$$

where $f(\xi)$ denotes the value of the target quantity evaluated at ξ, and ξ_0 denotes the original value of the parameter (Table 2, $\nu = 100$ mV s^{-1}, $\Psi = 1$ and $p = 1.013$ bar). Each parameter was varied by $\Delta\xi = \pm$ 10 %. Positive values of s_ξ indicate an increase in the current density by increasing the parameter ξ, and the opposite for negative values of s_ξ.

Among the parameters studied, the charge transfer coefficients were the most sensitive with relative sensitivities of –6.23 and –4.17 for α_{red,CO_2} and $\alpha_{form,CO}$. Their high sensitivity is attributed to their appearance in the exponential term of the rate equations. Their relative sensitivities are negative because α is defined for the anodic direction, while $(1-\alpha)$ is applied in the cathodic direction. Therefore, an increase in α leads to a decrease in the cathodic reaction rate and, consequently, a decrease in the cathodic current density.

The sensitivities of the rate constants are generally low, except for the CO_2 adsorption rate constant, k_{ads,CO_2}, which has a high sensitivity of 0.85. This high sensitivity is another evidence that CO_2 adsorption is rate-determining.

The surface roughness factor Ψ and the total pressure p have high positive relative sensitivities of 0.84 and 0.91, respectively. Therefore, we consider these parameters highly important and analyze them in more detail in the main manuscript.

Appendix B. Simulation Results at Different Scan Rates

A dynamic change in voltage, such as during a CV, affects sorption, reaction, and transport processes, and consequently, the resulting performance, i.e., current. As shown in Fig. 3, faster scan rates result in changes in the CV and higher peak current densities. In this section, we elucidate these changes with insights into the underlying processes, thus providing a more profound understanding of the dynamic interplay between the processes at the electrode surface. Fig. B.1 reveals the changes in the reaction rates (left) and surface coverages (right) with scan rates.

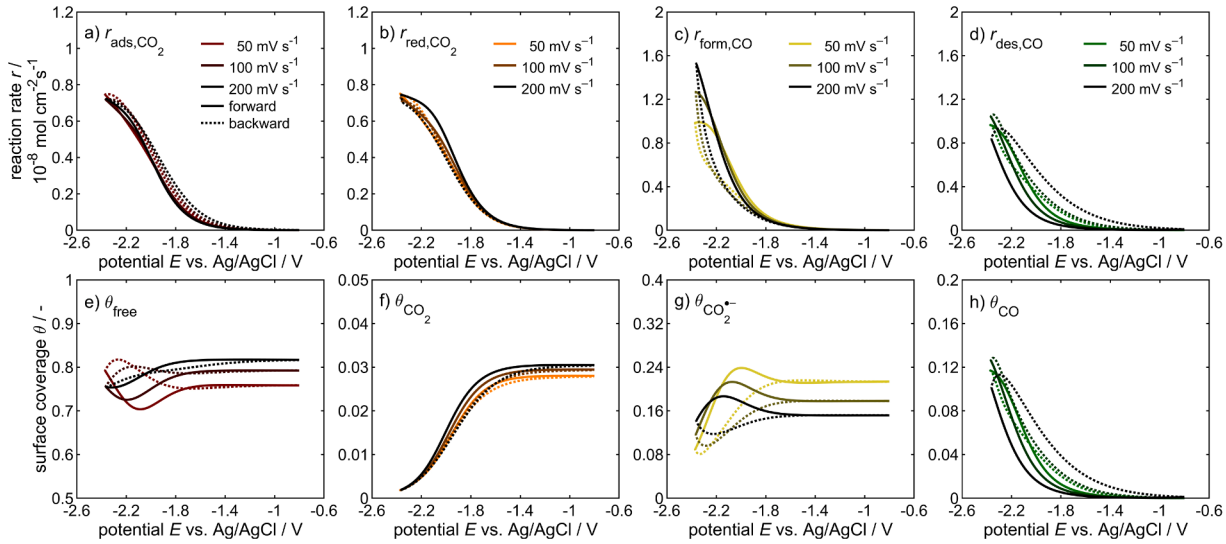

Fig. B.1. Impact of scan rate on reaction rates (a–d) and surface coverages (e–h) during cyclic voltammetry at scan rates of 50 mV s^{-1}, 100 mV s^{-1} and 200 mV s^{-1}: rates for CO_2 adsorption (a), CO_2 reduction (b), CO formation (c) and CO desorption (d); free surface (e), coverage with adsorbed CO_2 (f), adsorbed $CO_2^{\bullet-}$ (g) and adsorbed CO (h).

CO_2 adsorption and reduction rates follow a similar profile across all scan rates. The exponential slope during the forward sweep is slightly higher for 200 mV s^{-1}, leading to a more pronounced and earlier slowdown. Apart from this, they appear primarily independent of the scan rate. The rate of CO formation has a similar exponential slope across all scan rates during the forward sweep. In contrast, at lower cathodic potentials, the rate decelerates significantly at lower scan rates. During the backward sweep, the scan-rate dependence of CO formation disappears (Fig. B.1c).

The most notable impact of the scan rate is observed for CO desorption (Fig. B.1d): desorption rates are negligible above –1.8 V and exhibit an exponential increase afterward. This increase is delayed the higher the scan rate. This delay is continued at the beginning of the backward sweep, where the desorption rates for higher scan rates, particularly 200 mV s^{-1}, continue to increase briefly before gradually returning to their initial value. This behavior suggests that CO desorption is sluggish, lagging, and showing significant hysteresis with scan rate. However, its impact on performance is negligible, as evidenced by the observed increase in current with scan rate rather than a decrease. This lack of impact is attributed to CO desorption occurring after the irreversible electrochemical reactions, which are only indirectly influenced by slow CO desorption through the occupation of surface sites. The increase in peak current density at higher scan rates is primarily attributed to the increased electrochemical CO formation rate, as illustrated in Fig. 3c. Meanwhile, the rates of CO_2 adsorption and reduction remain essentially unaltered.

Fig. B.1e–h presents the simulated coverages of free surface sites (*) and adsorbates (*CO_2, *$CO_2^{\bullet-}$ and *CO) to examine the impact of dynamics on the surface and on the performance limitation. The surface coverages of free sites, Fig. B.1e, exhibit higher values at higher scan rates, and changes in slope become less pronounced, occurring at lower potentials for slower scan rates. Nevertheless, in all cases, 70 % of surface sites remain unoccupied at any given time.

The coverages of CO_2, Fig. B.1f, are largely unaffected by the scan rate, with a slightly delayed decrease for faster scan rates. However, the CO_2 coverage converges to the same low value at –2.3 V, indicating a performance limitation imposed by CO_2 adsorption in all cases.

The coverages of the CO_2 radical anion in Fig. B.1g show a substantial dependence on the scan rate, with lower coverages at faster scan rates for all potentials above –2.2 V. During the forward sweep, the maxima decrease and shift to more negative potentials at higher scan rates. Conversely, the coverage of $CO_2^{\bullet-}$ at the reversal point and the minima during the backward sweep increases with a higher scan rate. The relaxation during the backward sweep is faster for low scan rates, which ends up at higher $CO_2^{\bullet-}$ coverages at the start of each CV cycle: 16 % at 200 mV s^{-1} and 22 % at 50 mV s^{-1}. Even though above –2.2 V, the $CO_2^{\bullet-}$ coverages are lower at faster scan rates for all potentials, below –2.2 V, the $CO_2^{\bullet-}$ coverage remains higher at fast scan rates, thus enabling higher reaction rates for CO formation and consequently higher current densities.

The CO coverages (Fig. B.1h) exhibit a very similar profile to that of the rate of *CO desorption in Fig. B.1d: late exponential growth during the forward sweep followed by gradual relaxation during the backward sweep. As was already observed for the CO desorption rates, the CO coverage lags for fast scan rates.

In summary, the CO_2 surface coverage decreases and approaches depletion at potentials below –2.2 V, independent of the scan rate. We thus conclude once more that CO_2 adsorption is the rate-determining step for the overall reaction, and this to be independent of the scan rate. Despite this depletion of *CO_2, higher current densities are achieved at faster scan rates due to the higher residual coverage of $CO_2^{\bullet-}$ at potentials below –2.2 V.

Appendix C. Determination of the Roughness Factor

The surface roughness of the Cu electrodes was estimated from double layer capacitance measurements according to Verdaguer-Casadevall et al. based on cyclic voltammetry in the non-faradaic potential region [71]. The measurements were performed in the same electrochemical cell as the ambient pressure CVs with 1 mol L^{-1} NaOH electrolyte. The potential window was set to −0.45 V to −0.55 V vs. RHE for the planar Cu electrode and 0.35 V to 0.45 V vs. RHE for the Cu-NP electrode to avoid faradaic currents. Cycling was done at scan rates of 100 mV s^{-1}, 80 mV s^{-1}, 60 mV s^{-1}, 40 mV s^{-1}, and 20 mV s^{-1}.

The double layer capacitance C_{dl} was taken as the slope of the cathodic current density (in terms of geometric area) at the halfway potential (−0.5 V for the planar electrode, 0.4 V for the Cu-NP and 0.15 V for the Cu foil used in the high-pressure experiments) as a function of scan rate ν according to

$$j = C_{dl} \cdot \nu \tag{C.1}$$

Assuming proportionality between the double-layer capacitance C_{dl} and the number of active sites, the roughness factor Ψ can be estimated with reference to the polished polycrystalline planar Cu electrode according to

$$\Psi = \frac{C_{dl,Cu\text{-}NP}}{C_{dl,planar\ Cu}} \tag{C.2}$$

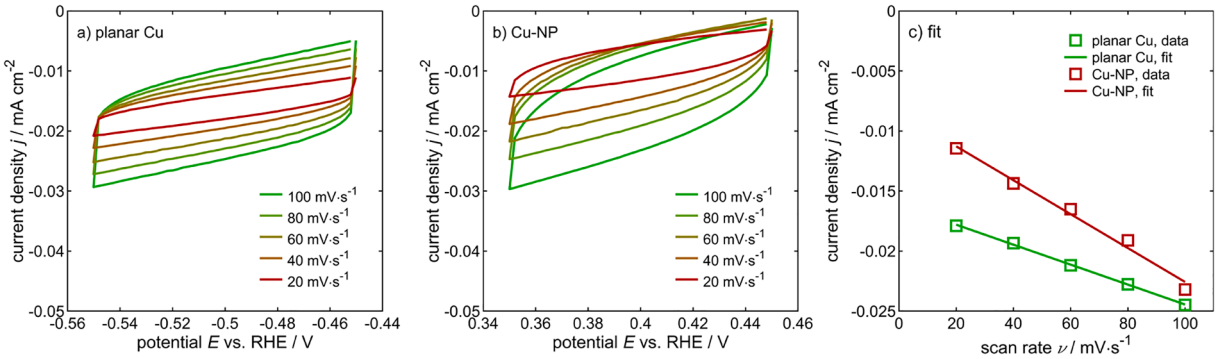

Fig. C.1. Estimation of roughness factor. Current densities versus potential at different scan rates for (a) planar Cu and (b) Cu-NP in 1 mol L^{-1} NaOH. (c) Capacitive current densities versus scan rate for Cu and Cu-NP. The estimated double layer capacitances are 0.0831 mF cm^{-2} and 0.1412 mF cm^{-2} for the planar Cu and Cu-NP electrodes. This yields a roughness factor of $\Psi = 1.699$ for the Cu-NP electrode.

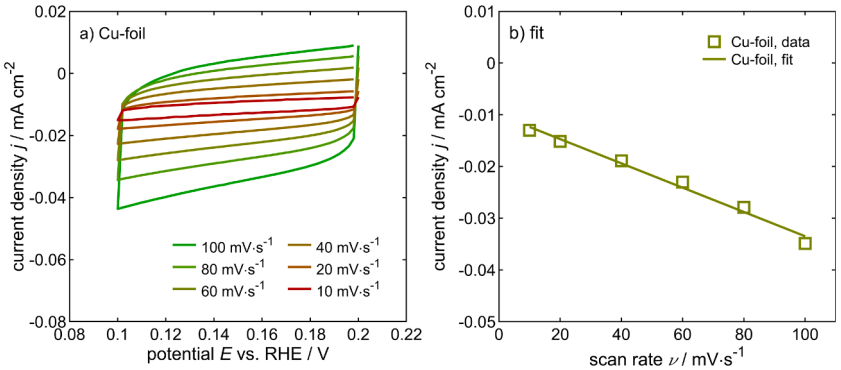

Fig. C.2. Estimation of roughness factor for the Cu foil used in high-pressure experiments. (a) Current densities versus potential at different scan rates in 1 mol L^{-1} NaOH. (b) Capacitive current densities versus scan rate. The estimated roughness factor with reference to the planar Cu electrode is $\Psi = 2.8244$.

Appendix D. Cyclic Voltammetry at Various Pressures

D1. Experimental Cyclic Voltammetry at Atmospheric Pressure

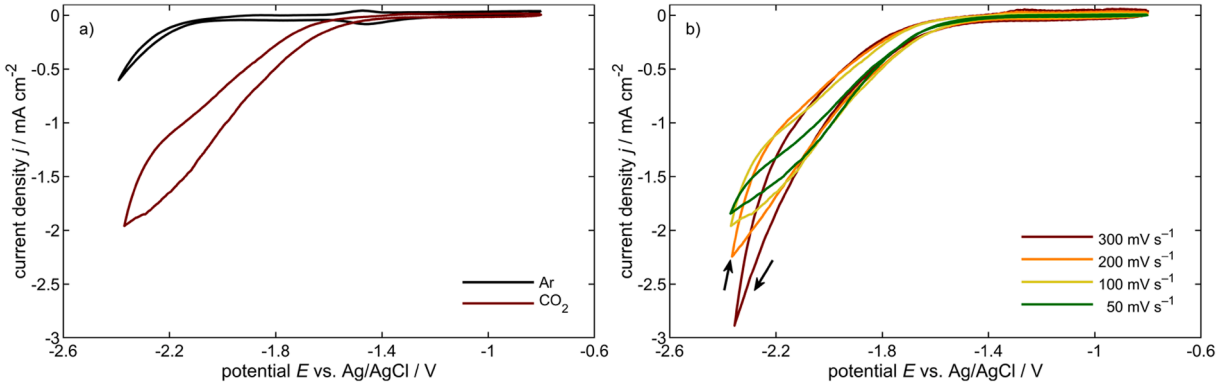

Fig. D.1. Experimental cyclic voltammograms of a planar Cu working electrode in 0.1 mol L^{-1} $TBABF_4$ in acetonitrile. a) Ar and CO_2 saturated electrolyte at 100 mV s^{-1} and b) scan rates 50–300 mV s^{-1} in CO_2 saturated electrolyte; *iR* corrected third cycle is shown.

D2. Cyclic Voltammetry at Sub-Atmospheric Pressure

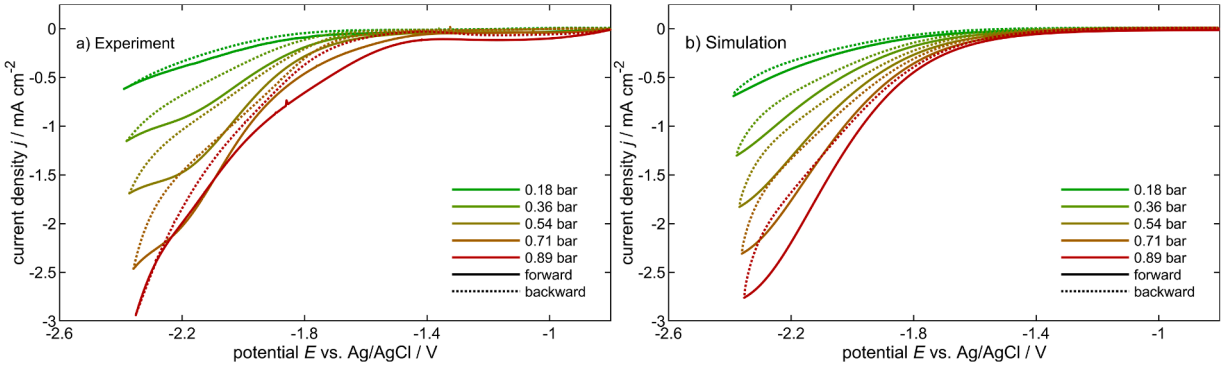

Fig. D.2. (a) Experimental and (b) simulated CVs under reduced CO_2 partial pressure (mixed CO_2/Ar atmosphere) with a planar Cu working electrode ($\Psi = 1.4$). The scan rate is 100 mV $^{s-1}$; iR-corrected third cycle is shown. The electrolyte is 0.1 mol L^{-1} $TBABF_4$ in acetonitrile. Cycling was done between −0.8 V and −2.0 V vs. Ag/AgCl (KCl_{sat} in H_2O). The solid line represents the forward, and the dotted line represents the backward sweep.

The experimental CVs recorded under sub-atmospheric conditions, as depicted in Fig. D.2a, exhibit consistent trends from 0.11 bar to 1.013 bar, characterized by an increase in peak current density with rising pressure, accompanied by a shift in the onset potential for the CO_2 reduction reaction towards less cathodic potentials. These observed experimental trends are in qualitative concurrence with the model predictions depicted in Fig. D.2b for a roughness factor of 1.4, which differs from $\Psi = 1$ of the planar Cu electrode used before, due to a complete repolish.

D3. Cyclic Voltammetry at Elevated Pressure

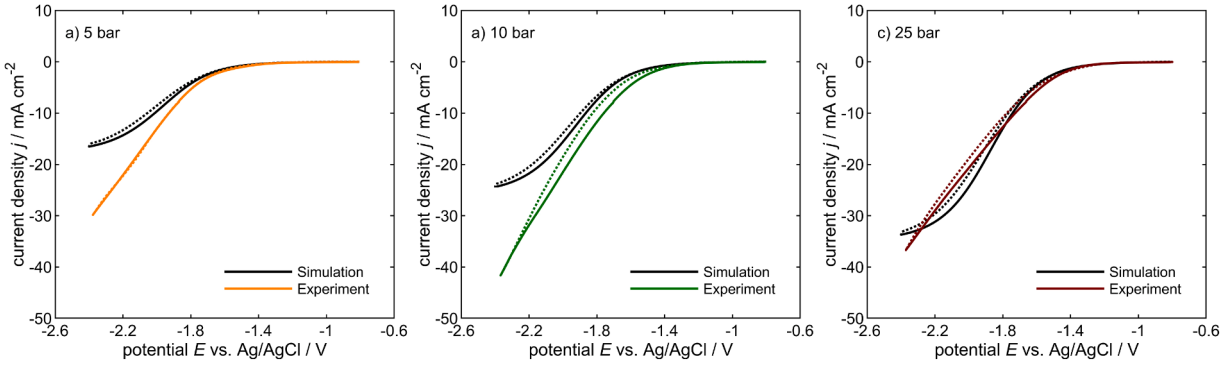

Fig. D.3. Comparison of experimental and simulated CVs under elevated pressure in the high-pressure cell. The scan rate is 100 mV s^{-1}; third cycle is shown. The electrolyte is 0.1 mol L^{-1} $TBABF_4$ in acetonitrile. Measurements were performed using 8 cm^2 Cu foil as the working electrode with an estimated roughness factor of $\Psi = 2.8244$ and a non-aqueous Ag/Ag^+ (0.1 mol L^{-1} $TBABF_4$ in acetonitrile) reference electrode. The shown potentials were converted to the Ag/AgCl (KCl_{sat} in H_2O) reference electrode used in the other measurements. Cycling was done between −0.8 V and −2.4 V vs. Ag/AgCl (KCl_{sat} in H_2O). The solid line represents the forward, and the dotted line represents the backward sweep.

Fig. D.3 presents the experimental and simulated CVs from 5 bar to 25 bar. At 5 bar and 10 bar, the trend of an increase in current density and a shift to lower onset potentials for the CO_2 reduction as the pressure increases persists. However, at 25 bar, we observe a significant departure from this pattern, as discussed in the main text.

Table D.1
Additional parameter values for the CV simulations at 5 bar, 10 bar and 25 bar pressure. CO_2 solubilities are calculated via Henry's law with Henry coefficient of CO_2 in acetonitrile given in Table 1. Uncompensated internal resistance R_u is experimentally determined via EIS. RMSE represent the goodness of fit between the third cycle of the experimental and simulated cyclic voltammograms.

Total pressure in bar	$c_{CO_2,max}$ in kmol L^{-1}	R_u in Ω	RMSE in mA cm^{-2}
5	1.520	1.36	4.294
10	3.077	1.37	5.436
25	7.746	1.50	1.7501

References

[1] S. Nitopi, E. Bertheussen, S.B. Scott, X. Liu, A.K. Engstfeld, S. Horch, B. Seger, I.E. L. Stephens, K. Chan, C. Hahn, J.K. Nørskov, T.F. Jaramillo, I. Chorkendorff, Progress and perspectives of electrochemical CO2 reduction on copper in aqueous electrolyte, Chem. Rev. 119 (2019) 7610–7672, https://doi.org/10.1021/acs.chemrev.8b00705.

[2] A. Gawel, T. Jaster, D. Siegmund, J. Holzmann, H. Lohmann, E. Klemm, U.P. Apfel, Electrochemical CO2 reduction - the macroscopic world of electrode design, reactor concepts & economic aspects, iScience 25 (2022) 104011, https://doi.org/10.1016/j.isci.2022.104011.

[3] M.M.de S. Pupo, R. Kortlever, Electrolyte effects on the electrochemical reduction of CO2, ChemPhysChem 20 (2019) 2926–2935, https://doi.org/10.1002/cphc.201900680.

[4] G. Marcandalli, M.C.O. Monteiro, A. Goyal, M.T.M. Koper, Electrolyte effects on CO2 electrochemical reduction to CO, Acc. Chem. Res. 55 (2022) 1900–1911, https://doi.org/10.1021/acs.accounts.2c00080.

[5] Y.Y. Birdja, E. Pérez-Gallent, M.C. Figueiredo, A.J. Göttle, F. Calle-Vallejo, M.T. M. Koper, Advances and challenges in understanding the electrocatalytic conversion of carbon dioxide to fuels, Nat. Energy 4 (2019) 732–745, https://doi.org/10.1038/s41560-019-0450-y.

[6] I.E.L. Stephens, K. Chan, A. Bagger, S.W. Boettcher, J. Bonin, E. Boutin, A. K. Buckley, R. Buonsanti, E.R. Cave, X. Chang, S.W. Chee, A.H.M. da Silva, P. de Luna, O. Einsle, B. Endrődi, M. Escudero-Escribano, J.V.F. de Araujo, M. C. Figueiredo, C. Hahn, K.U. Hansen, S. Haussener, S. Hunegnaw, Z. Huo, Y. J. Hwang, C. Janáky, B.S. Jayathilake, F. Jiao, Z.P. Jovanov, P. Karimi, M.T. M. Koper, K.P. Kuhl, W.H. Lee, Z. Liang, X. Liu, S. Ma, M. Ma, H.S. Oh, M. Robert, B.R. Cuenya, J. Rossmeisl, C. Roy, M.P. Ryan, E.H. Sargent, P. Sebastián-Pascual, B. Seger, L. Steier, P. Strasser, A.S. Varela, R.E. Vos, X. Wang, B. Xu, H. Yadegari, Y. Zhou, Roadmap on low temperature electrochemical CO2 reduction, J. Phys. Energy 4 (2022) 042003, https://doi.org/10.1088/2515-7655/ac7823.

[7] S. Popović, M. Smiljanić, P. Jovanovič, J. Vavra, R. Buonsanti, N. Hodnik, Stability and degradation mechanisms of copper-based catalysts for electrochemical CO2 reduction, Angew. Chem. Int. Ed. 59 (2020) 14736–14746, https://doi.org/10.1002/anie.202000617.

[8] J. Vavra, T.H. Shen, D. Stoian, V. Tileli, R. Buonsanti, Real-time monitoring reveals dissolution/redeposition mechanism in copper nanocatalysts during the initial stages of the CO2 reduction reaction, Angew. Chem. Int. Ed. 60 (2021) 1347–1354, https://doi.org/10.1002/anie.202011137.

[9] T. Jaster, S. Albers, A. Leonhard, M.A. Kräenbring, H. Lohmann, B. Zeidler-Fandrich, F. Özcan, D. Segets, U.P. Apfel, Enhancement of CO2RR product formation on Cu-ZnO-based electrodes by varying ink formulation and post-treatment methods, J. Phys. Energy 5 (2023) 024001, https://doi.org/10.1088/2515-7655/acb8db.

[10] A.R. Woldu, Z. Huang, P. Zhao, L. Hu, D. Astruc, Electrochemical CO2 reduction (CO2RR) to multi-carbon products over copper-based catalysts, Coord. Chem. Rev. 454 (2022) 214340, https://doi.org/10.1016/j.ccr.2021.214340.

[11] P.P. Yang, M.R. Gao, Enrichment of reactants and intermediates for electrocatalytic CO 2 reduction, Chem. Soc. Rev. 52 (2023) 4343–4380, https://doi.org/10.1039/D2CS00849A.

[12] A. Goyal, G. Marcandalli, V.A. Mints, M.T.M. Koper, Competition between CO2 reduction and hydrogen evolution on a gold electrode under well-defined mass transport conditions, J. Am. Chem. Soc. 142 (2020) 4154–4161, https://doi.org/10.1021/jacs.9b10061.

[13] B.J.M. Etzold, U. Krewer, S. Thiele, A. Dreizler, E. Klemm, T. Turek, Understanding the activity transport nexus in water and CO2 electrolysis: state of the art, challenges and perspectives, Chem. Eng. J. 424 (2021) 130501, https://doi.org/10.1016/j.cej.2021.130501.

[14] J.A. Rabinowitz, M.W. Kanan, The future of low-temperature carbon dioxide electrolysis depends on solving one basic problem, Nat. Commun. 11 (2020) 5231, https://doi.org/10.1038/s41467-020-19135-8.

[15] Y. Xie, P. Ou, X. Wang, Z. Xu, Y.C. Li, Z. Wang, J.E. Huang, J. Wicks, C. McCallum, N. Wang, Y. Wang, T. Chen, B.T.W. Lo, D. Sinton, J.C. Yu, Y. Wang, E.H. Sargent, High carbon utilization in CO2 reduction to multi-carbon products in acidic media, Nat. Catal. (2022) 1–7, https://doi.org/10.1038/s41929-022-00788-1.

[16] H. Ooka, M.C. Figueiredo, M.T.M. Koper, Competition between hydrogen evolution and carbon dioxide reduction on copper electrodes in mildly acidic media, Langmuir 33 (2017) 9307–9313, https://doi.org/10.1021/acs.langmuir.7b00696.

[17] A. Bagger, W. Ju, A.S. Varela, P. Strasser, J. Rossmeisl, Single site porphyrine-like structures advantages over metals for selective electrochemical CO2 reduction, Catal. Today 288 (2017) 74–78, https://doi.org/10.1016/j.cattod.2017.02.028.

[18] R. Kortlever, J. Shen, K.J.P. Schouten, F. Calle-Vallejo, M.T.M. Koper, Catalysts and reaction pathways for the electrochemical reduction of carbon dioxide, J. Phys. Chem. Lett. 6 (2015) 4073–4082, https://doi.org/10.1021/acs.jpclett.5b01559.

[19] A.V. Rudnev, U.E. Zhumaev, A. Kuzume, S. Vesztergom, J. Furrer, P. Broekmann, T. Wandlowski, The promoting effect of water on the electroreduction of CO2 in acetonitrile, Electrochim. Acta 189 (2016) 38–44, https://doi.org/10.1016/j.electacta.2015.12.088.

[20] A.T. Chu, Y. Surendranath, Aprotic solvent exposes an altered mechanism for copper-catalyzed ethylene electrosynthesis, J. Am. Chem. Soc. 144 (2022) 5359–5365, https://doi.org/10.1021/jacs.1c12595.

[21] K. Ito, S. Ikeda, T. Iida, A. Nomura, Electrochemical reduction of carbon dioxide dissolved under high pressure III. In nonaqueous electrolytes, Denki Kagaku Oyobi Kogyo Butsuri Kagaku 50 (1982) 463–469, https://doi.org/10.5796/kogyobutsurikagaku.50.463.

[22] K. Ito, S. Ikeda, N. Yamauchi, T. Iida, T. Takagi, Electrochemical reduction products of carbon dioxide at some metallic electrodes in nonaqueous electrolytes, Bull. Chem. Soc. Jpn. 58 (1985) 3027–3028, https://doi.org/10.1246/bcsj.58.3027.

[23] S. Ikeda, T. Takagi, K. Ito, Selective formation of formic acid, oxalic acid, and carbon monoxide by electrochemical reduction of carbon dioxide, Bull. Chem. Soc. Jpn. 60 (1987) 2517–2522, https://doi.org/10.1246/bcsj.60.2517.

[24] T.C. Berto, L. Zhang, R.J. Hamers, J.F. Berry, Electrolyte dependence of CO2 electroreduction: tetraalkylammonium ions are not electrocatalysts, ACS Catal. 5 (2015) 703–707, https://doi.org/10.1021/cs501641z.

[25] Á. Díaz-Duque, A.P. Sandoval-Rojas, A.F. Molina-Osorio, J.M. Feliu, M.F. Suárez-Herrera, Electrochemical reduction of CO2 in water-acetonitrile mixtures on nanostructured Cu electrode, Electrochem. Commun. 61 (2015) 74–77, https://doi.org/10.1016/j.elecom.2015.10.003.

[26] A.V. Rudnev, M.R. Ehrenburg, E.B. Molodkina, I.G. Botriakova, A.I. Danilov, T. Wandlowski, CO2 Electroreduction on Cu-modified platinum single crystal electrodes in aprotic media, Electrocatalysis 6 (2015) 42–50, https://doi.org/10.1007/s12678-014-0217-y.

[27] S. Piontek, K. junge Puring, D. Siegmund, M. Smialkowski, I. Sinev, D. Tetzlaff, B. R. Cuenya, U.P. Apfel, Bio-inspired design: bulk iron–nickel sulfide allows for efficient solvent-dependent CO 2 reduction, Chem. Sci. 10 (2019) 1075–1081, https://doi.org/10.1039/C8SC03555E.

[28] M. König, S.H. Lin, J. Vaes, D. Pant, E. Klemm, Integration of aprotic CO2 reduction to oxalate at a Pb catalyst into a GDE flow cell configuration, Faraday Discuss 230 (2021) 360–374, https://doi.org/10.1039/D0FD00141D.

[29] R.J. Gomes, C. Birch, M.M. Cencer, C. Li, S.B. Son, I.D. Bloom, R.S. Assary, C. V. Amanchukwu, Probing electrolyte influence on CO2 reduction in aprotic solvents, J. Phys. Chem. C 126 (2022) 13595–13606, https://doi.org/10.1021/acs.jpcc.2c03321.

[30] B.A. Rohr, A.R. Singh, J.A. Gauthier, M.J. Statt, J.K. Nørskov, Micro-kinetic model of electrochemical carbon dioxide reduction over platinum in non-aqueous solvents, Phys. Chem. Chem. Phys. 22 (2020) 9040–9045, https://doi.org/10.1039/C9CP05751J.

[31] A. Bagger, O. Christensen, V. Ivaništšev, J. Rossmeisl, Catalytic CO2/CO reduction: gas, aqueous, and aprotic phases, ACS Catal. 12 (2022) 2561–2568, https://doi.org/10.1021/acscatal.1c05358.

[32] V. Boor, J.E.B.M. Frijns, E. Perez-Gallent, E. Giling, A.T. Laitinen, E.L.V. Goetheer, L.J.P. van den Broeke, R. Kortlever, W. de Jong, O.A. Moultos, T.J.H. Vlugt, M. Ramdin, Electrochemical reduction of CO2 to oxalic acid: experiments, process modeling, and economics, Ind. Eng. Chem. Res. (2022), https://doi.org/10.1021/acs.iecr.2c02647.

[33] M. König, J. Vaes, D. Pant, E. Klemm, Effect of solvents on aprotic CO2 reduction: a study on the role of CO2 mass transport in the product selectivity between oxalate and carbon monoxide, J. Phys. Chem. C (2023), https://doi.org/10.1021/acs.jpcc.3c03992.

[34] K.F. Kalz, R. Kraehnert, M. Dvoyashkin, R. Dittmeyer, R. Gläser, U. Krewer, K. Reuter, J.D. Grunwaldt, Future challenges in heterogeneous catalysis: understanding catalysts under dynamic reaction conditions, ChemCatChem 9 (2017) 17–29, https://doi.org/10.1002/cctc.201600996.

[35] U. Kaiser, E. Heitz, Zum mechanismus der elektrochemischen dimerisierung von CO2 zu Oxalsäure, Berichte Bunsenges. Für Phys. Chem. 77 (1973) 818–823, https://doi.org/10.1002/bbpc.19730771018.

[36] M.C. Figueiredo, I. Ledezma-Yanez, M.T.M. Koper, In situ spectroscopic study of CO2 electroreduction at copper electrodes in acetonitrile, ACS Catal. 6 (2016) 2382–2392, https://doi.org/10.1021/acscatal.5b02543.

[37] J. Shi, F. Shen, F. Shi, N. Song, Y.J. Jia, Y.Q. Hu, Q.Y. Li, J. Liu, T.Y. Chen, Y.N. Dai, Electrochemical reduction of CO2 into CO in tetrabutylammonium perchlorate/propylene carbonate: water effects and mechanism, Electrochim. Acta 240 (2017) 114–121, https://doi.org/10.1016/j.electacta.2017.04.065.

[38] P.B. Joshi, N. Karki, A.J. Wilson, Electrocatalytic CO2 reduction in acetonitrile enhanced by the local environment and mass transport of H2O, ACS Energy Lett. (2022) 602–609, https://doi.org/10.1021/acsenergylett.1c02667.

[39] C. Amatore, J.M. Savéant, Mechanism and kinetic characteristics of the electrochemical reduction of carbon dioxide in media of low proton availability, J. Am. Chem. Soc. 103 (1981) 5021–5023, https://doi.org/10.1021/ja00407a008.

[40] M. König, J. Vaes, E. Klemm, D. Pant, Solvents and supporting electrolytes in the electrocatalytic reduction of CO2, iScience 19 (2019) 135–160, https://doi.org/10.1016/j.isci.2019.07.014.

[41] S. Garg, M. Li, A.Z. Weber, L. Ge, L. Li, V. Rudolph, G. Wang, T.E. Rufford, Advances and challenges in electrochemical CO2 reduction processes: an engineering and design perspective looking beyond new catalyst materials, J. Mater. Chem. A 34 (2020), https://doi.org/10.1039/C9TA13298H.

[42] A. Gennaro, A.A. Isse, E. Vianello, Solubility and electrochemical determination of CO2 in some dipolar aprotic solvents, J. Electroanal. Chem. Interfacial Electrochem. 289 (1990) 203–215, https://doi.org/10.1016/0022-0728(90)87217-8.

[43] D. Niu, H. Wang, H. Li, X. Zhang, The effect of the alkyl chain length of the tetraalkylammonium cation on CO2 electroreduction in an aprotic medium, Electrochem. Commun. 52 (2015) 58–62, https://doi.org/10.1016/j.elecom.2015.01.022.

[44] J. Geppert, F. Kubannek, P. Röse, U. Krewer, Identifying the oxygen evolution mechanism by microkinetic modelling of cyclic voltammograms, Electrochim. Acta 380 (2021) 137902, https://doi.org/10.1016/j.electacta.2021.137902.

[45] J. Geppert, P. Röse, S. Pauer, U. Krewer, Microkinetic barriers of the oxygen evolution on the oxides of iridium, ruthenium and their binary mixtures, ChemElectroChem 9 (2022) e202200481, https://doi.org/10.1002/celc.202200481.

[46] M. Röhe, F. Kubannek, U. Krewer, Processes and their limitations in oxygen depolarized cathodes: a dynamic model-based analysis, ChemSusChem 12 (2019) 2373–2384, https://doi.org/10.1002/cssc.201900312.

[47] I. Dorner, P. Röse, U. Krewer, Dynamic vs. Stationary analysis of electrochemical carbon dioxide reduction: profound differences in local states, ChemElectroChem 10 (2023) e202300387, https://doi.org/10.1002/celc.202300387.

[48] T. Haisch, F. Kubannek, L. Nikitina, I. Nikitin, S. Pott, T. Clees, U. Krewer, The origin of the hysteresis in cyclic voltammetric response of alkaline methanol electrooxidation, Phys. Chem. Chem. Phys. 22 (2020) 16648–16654, https://doi.org/10.1039/D0CP00976H.

[49] J. Geppert, P. Röse, S. Czioska, D. Escalera-López, A. Boubnov, E. Saraçi, S. Cherevko, J.D. Grunwaldt, U. Krewer, Microkinetic analysis of the oxygen evolution performance at different stages of iridium oxide degradation, J. Am. Chem. Soc. 144 (2022) 13205–13217, https://doi.org/10.1021/jacs.2c03561.
[50] K. Junge Puring, O. Evers, M. Prokein, D. Siegmund, F. Scholten, N. Mölders, M. Renner, B. Roldan Cuenya, M. Petermann, E. Weidner, U.P. Apfel, Assessing the influence of supercritical carbon dioxide on the electrochemical reduction to formic acid using carbon-supported copper catalysts, ACS Catal. 10 (2020) 12783–12789, https://doi.org/10.1021/acscatal.0c02983.
[51] M.T. Tyn, W.F. Calus, Diffusion coefficients in dilute binary liquid mixtures, J. Chem. Eng. Data 20 (1975) 106–109, https://doi.org/10.1021/je60064a006.
[52] A.J. Bard, L.R. Faulkner, H.S. White, Electrochemical Methods: Fundamentals and Applications, 3rd ed., Wiley, Hoboken, NJ, 2022.
[53] E.J.F. Dickinson, J.G. Limon-Petersen, N.V. Rees, R.G. Compton, How much supporting electrolyte is required to make a cyclic voltammetry experiment quantitatively "diffusional"? A theoretical and experimental investigation, J. Phys. Chem. C 113 (2009) 11157–11171, https://doi.org/10.1021/jp901628h.
[54] R. Guidelli, R.G. Compton, J.M. Feliu, E. Gileadi, J. Lipkowski, W. Schmickler, S. Trasatti, Defining the transfer coefficient in electrochemistry: an assessment (IUPAC Technical Report), Pure Appl. Chem. 86 (2014) 245–258, https://doi.org/10.1515/pac-2014-5026.
[55] P. Schön, U. Krewer, Revealing the complex sulfur reduction mechanism using cyclic voltammetry simulation, Electrochim. Acta 373 (2021) 137523, https://doi.org/10.1016/j.electacta.2020.137523.
[56] C. Deacon-Price, A.H.M. da Silva, C.S. Santana, M.T.M. Koper, A.C. Garcia, Solvent effect on electrochemical CO2 reduction reaction on nanostructured copper electrodes, J. Phys. Chem. C (2023), https://doi.org/10.1021/acs.jpcc.3c03257.
[57] A.W.B. Aylmer-Kelly, A. Bewick, P.R. Cantrill, A.M. Tuxford, Studies of electrochemically generated reaction intermediates using modulated specular reflectance spectroscopy, Faraday Discuss. Chem. Soc. 56 (1973) 96–107, https://doi.org/10.1039/DC9735600096.
[58] Yu.B. Vassiliev, V.S. Bagotzky, O.A. Khazova, N.A. Mayorova, Electroreduction of carbon dioxide: part II. The mechanism of reduction in aprotic solvents, J. Electroanal. Chem. 189 (1985) 295–309, https://doi.org/10.1016/0368-1874(85)80074-5.
[59] F. You, S. Xi, J.J.Y. Ho, F. Calle-Vallejo, B.S. Yeo, Influence of copper sites with different coordination on the adsorption and electroreduction of CO_2 and CO, ACS Catal. (2023) 11136–11143, https://doi.org/10.1021/acscatal.3c03197.
[60] J.A. Gauthier, M. Fields, M. Bajdich, L.D. Chen, R.B. Sandberg, K. Chan, J. K. Nørskov, Facile Electron Transfer to CO2 during Adsorption at the Metal| Solution Interface, J. Phys. Chem. C 123 (2019) 29278–29283, https://doi.org/10.1021/acs.jpcc.9b10205.
[61] T. Jaster, A. Gawel, D. Siegmund, J. Holzmann, H. Lohmann, E. Klemm, U.P. Apfel, Electrochemical CO2 reduction toward multicarbon alcohols - the microscopic world of catalysts & process conditions, iScience 25 (2022) 104010, https://doi.org/10.1016/j.isci.2022.104010.
[62] K. Jiang, Y. Huang, G. Zeng, F.M. Toma, W.A. Goddard, A.T. Bell, Effects of surface roughness on the electrochemical reduction of CO2 over Cu, ACS Energy Lett. 5 (2020) 1206–1214, https://doi.org/10.1021/acsenergylett.0c00482.
[63] K.R. Ward, M. Gara, N.S. Lawrence, R.S. Hartshorne, R.G. Compton, Nanoparticle modified electrodes can show an apparent increase in electrode kinetics due solely to altered surface geometry: the effective electrochemical rate constant for non-flat and non-uniform electrode surfaces, J. Electroanal. Chem. 695 (2013) 1–9, https://doi.org/10.1016/j.jelechem.2013.02.012.
[64] A.H.M. da Silva, S.J. Raaijman, C.S. Santana, J.M. Assaf, J.F. Gomes, M.T.M. Koper, Electrocatalytic CO2 reduction to C2+ products on Cu and CuxZny electrodes: effects of chemical composition and surface morphology, J. Electroanal. Chem. 880 (2021) 114750, https://doi.org/10.1016/j.jelechem.2020.114750.
[65] L.A. Zook, J. Leddy, Density and solubility of nafion: recast, annealed, and commercial films, Anal. Chem. 68 (1996) 3793–3796, https://doi.org/10.1021/ac960604e.
[66] C. Punckt, M.A. Pope, I.A. Aksay, On the electrochemical response of porous functionalized graphene electrodes, J. Phys. Chem. C 117 (2013) 16076–16086, https://doi.org/10.1021/jp405142k.
[67] C.I. Shaughnessy, D.J. Sconyers, T.A. Kerr, H.J. Lee, B. Subramaniam, K. C. Leonard, J.D. Blakemore, Intensified Electrocatalytic CO2 conversion in pressure-tunable CO2-expanded electrolytes, ChemSusChem 12 (2019) 3761–3768, https://doi.org/10.1002/cssc.201901107.
[68] D.J. Sconyers, C.I. Shaughnessy, H.J. Lee, B. Subramaniam, K.C. Leonard, J. D. Blakemore, Enhancing molecular electrocatalysis of CO2 reduction with pressure-tunable CO2-expanded electrolytes, ChemSusChem 13 (2020) 6338–6345, https://doi.org/10.1002/cssc.202000390.
[69] C.K. Nilles, A.K. Borkowski, E.R. Bartlett, M.A. Stalcup, H.J. Lee, K.C. Leonard, B. Subramaniam, W.H. Thompson, J.D. Blakemore, Mechanistic basis of conductivity in carbon dioxide-expanded electrolytes: a joint experimental–theoretical study, J. Am. Chem. Soc. 146 (2024) 2398–2410, https://doi.org/10.1021/jacs.3c08145.
[70] O. Melchaeva, P. Voyame, V.C. Bassetto, M. Prokein, M. Renner, E. Weidner, M. Petermann, A. Battistel, Electrochemical reduction of protic supercritical CO2 on copper electrodes, ChemSusChem 10 (2017) 3660–3670, https://doi.org/10.1002/cssc.201701205.
[71] A. Verdaguer-Casadevall, C.W. Li, T.P. Johansson, S.B. Scott, J.T. McKeown, M. Kumar, I.E.L. Stephens, M.W. Kanan, I. Chorkendorff, Probing the active surface sites for CO reduction on oxide-derived copper electrocatalysts, J. Am. Chem. Soc. 137 (2015) 9808–9811, https://doi.org/10.1021/jacs.5b06227.